Improved 3D Modelling of CANDU Reactors Using Transport-Fitted Diffusion Coefficients

Ashlea V. K. Colton

A Thesis Submitted in Partial Fulfilment of the Requirements for the Degree of

Masters of Science

in

the Faculty of Science

Modelling and Computational Science

Program

University of Ontario Institute of Technology

December 2016

ABSTRACT

To model the neutronic physics behavior of the core in CANDU pressure tube type heavy water reactors with natural-uranium fuel, two levels of calculations are required. Initially, lattice-level transport calculations are carried out to obtain, with high detail and accuracy, the flux distribution inside the lattice cell and composition of the nuclear fuel. Lattice calculations use many (30- 180) energy groups and detailed geometric information to model the fuel channel and the fuel contained within.

Once the lattice calculations are complete, the fuel compositions obtained can be used to generate cell-homogenized macroscopic cross-sections condensed to two energy groups, for use in full-core diffusion calculations. Two-group cell-homogenized cross-sections work to acceptable levels of accuracy in most full-core configurations. However, challenges appear when modelling the neutron flux at the fuel-reflector interface (at the boundary of the reactor).

This work aims to improve the neutron flux estimates obtained in three-dimensional diffusion calculations by using diffusion coefficients fitted to transport results. It will be shown that significant improvements (>10%) can be made for modeling the neutron physics at the core-reflector interface.

Keywords: Reactor Physics, Diffusion Equation

ACKNOWLEDGMENTS

I am indebted to Dr. Eleodor Nichita for accepting me as a part time graduate student and for providing his insights and guidance along the way. His patience, knowledge and sense of humor are deeply appreciated. This work has placed many demands on my family, as every hour writing and analyzing was an hour away from them. To my husband, Alexi Shkarupin, I am grateful for his support and encouragement. To both my children, Abbey and Axel, I am thankful for the inspiration they provide. Thanks to my mother, Wendy Colton for instilling in me a desire to attend post-secondary education in the first place. This work has been positively influenced by Blair Bromley and Sourena Golesorkhi through their kind review. I greatly appreciate my managers for their patience and flexibility without which this degree would not have been possible. To Dr. Adriaan Buijs, my first manager, I offer my gratitude for being accommodating of my study schedule and for encouraging me to work and study. Thanks to Jim Sullivan, who gave me the opportunity to come to Chalk River Laboratories. Lastly, my utmost appreciation to Dr. Darren D. Radford, who has been a strong supporting and encouraging force in my life.

Were it not for Dr. Ruth Lavergne and her outstanding academic accomplishments, I might not have believed it possible to juggle work, education and children. Thanks to Bronwyn Hyland for being a friend who helped me focus on the path to achieving my goals and not on the obstacles in the way. To Laura Blomeley, my office sister, I am grateful for our conversations. Thanks for being there.

TABLE OF CONTENTS

ABSTRACT II

ACKNOWLEDGMENTS III

TABLE OF CONTENTS IV

LIST OF TABLES VI

LIST OF FIGURES VII

LIST OF SYMBOLS IX

1. INTRODUCTION 1

1.1 CANDU Reactor Description 1

1.2 Microscopic and Macroscopic Nuclear Cross-Sections 4

1.3 CANDU Modelling Summary 6

1.4 Review of Homogenization Techniques 8

1.5 Research Motivation 9

1.1 Objective 10

2. METHODS 12

2.1 The Neutron Transport Equation 12

2.2 The Diffusion Approximation 16

2.3 The Two-Group Diffusion Equation 19

2.4 Deriving the Diffusion Coefficients from the Transport Solution 21

2.5 Description of Nuclear Data and Codes Used 24
2.5.1 DRAGON 24
2.5.2 DONJON 25

2.6 Description of Physics Models Prepared 26
2.6.1 Lattice Physics Models 26
2.6.1 Multicell Models 31
2.6.2 Evaluation Metrics for Multicell Cases 38

3. RESULTS 39

3.1 Homogeneous, One-Dimensional, Diffusion-Coefficient-Derivation Case 39

3.2 Homogeneous, One-Dimensional Coolant Voided Case 44

3.3 Heterogeneous, One-Dimensional Case 46

3.4 Heterogeneous, Two-Dimensional Case 51

3.5 Heterogeneous, Three-Dimensional Case 55

4. CONCLUSIONS 61

5. REFERENCES 63

APPENDIX A: MESH REFINEMENT STUDY 65

X Mesh Convergence Study 65

Z-Mesh Convergence Study 66

LIST OF TABLES

Table 1: Lattice Cell Geometric Parameters for Nominal and Cartesian Geometries 26

Table 2: Lattice Temperature and Density Parameters 28

Table 3: Multicell Cases to be Modelled 32

Table 4: Results of Homogeneous, One-Dimensional Case 43

Table 5: Results of Homogeneous, 1-D Voided Case 45

Table 6: Results of Heterogeneous, One-Dimensional Case 50

Table 7: BlackStallion Results for Heterogeneous, 1-D Case (Patel, 2010) 50

Table 8: Results Summary for Heterogeneous, 2-D Case 55

Table 9: Fast Flux % Difference from DONJON for 3D Heterogeneous Case 56

Table 10: Fast Flux % Difference from DONJON(tr) for 3D Heterogeneous Case 57

Table 11: Thermal Flux % Difference from DONJON for 3D Heterogeneous Case 57

Table 12: Thermal Flux % Difference from DONJON (tr) for 3D Heterogeneous Case 58

Table 13: Fission Rate Difference from DONJON for 3D Heterogeneous Case 58

Table 14: Fission Rate Difference from DONJON(tr) for 3D Heterogeneous Case 59

Table 15: Results of Three-Dimensional, Heterogeneous Case 59

LIST OF FIGURES

Figure 1: Pressure Tube Heavy Water Reactor (Rosana, 2014)..... 1

Figure 2: 37-Element Fuel Bundle (Page, 2012)..... 2

Figure 3: Atom Density in atoms/barn·cm of Important Isotopes as a function of Burn-up for Natural Uranium Fuel (Yasin, Iqbal, & Shahzad, 2011)..... 4

Figure 4: U-235 Fission Cross-Section (Chadwick, 2011)..... 5

Figure 5: 37-Element CANDU Lattice Cell (Hangbok, Gyuhong, & Donghwan, 2005)..... 7

Figure 6: Example Elements for Estimating Flux Laplacian..... 22

Figure 7: Example Elements for Estimating Flux Laplacian at Reflective Boundary..... 23

Figure 8: Example Elements for Estimating Flux Laplacian at Vacuum Boundary..... 24

Figure 9: Data Flow of Physics Analysis Performed..... 26

Figure 10: Lattice Cell Cluster Geometry (left) and Cartesian Geometry (right)..... 29

Figure 11: Reactor Face Layout..... 34

Figure 12: 1-D Homogeneous Case Geometry..... 34

Figure 13: 1-D Heterogeneous Case Geometry..... 35

Figure 14: 2-D Heterogeneous Case Geometry..... 36

Figure 15: 3-D Heterogeneous Case Geometry..... 37

Figure 16: Spatial Dependence of One-Dimensional-Derived Diffusion Coefficients..... 40

Figure 17: Percent Difference in Flux for the Homogeneous, 1-D Case..... 41

Figure 18: Percent Difference in Fission Rate for the Homogeneous, 1-D Case..... 42

Figure 19: Flux for the Homogeneous, One-Dimensional Case..... 43

Figure 20: Fission Rate for Homogeneous, 1-D, Coolant Void Case..... 45

Figure 21: Flux for Heterogeneous, 1-D Case 46

Figure 22: DRAGON Flux Laplacian for Heterogeneous, 1-D Case 48

Figure 23: Percent Difference in Flux for Heterogeneous, 1-D Case 48

Figure 24: Percent Difference in Fission Rate for Heterogeneous, 1-D Case 49

Figure 25: DRAGON Fast Flux for Heterogeneous, 2-D Case 51

Figure 26: DRAGON Thermal Flux for Heterogeneous, 2-D Case 51

Figure 27: DONJON Fast Flux Percent Differences for Heterogeneous, 2-D Case 52

Figure 28: DONJON(tr) Fast Flux Percent Differences for Heterogeneous, 2-D Case 52

Figure 29: DONJON Thermal Flux Percent Difference for Heterogeneous, 2-D Case 53

Figure 30: DONJON (tr) Thermal Flux Percent Difference for Heterogeneous, 2-D Case 53

Figure 31: DONJON Fission Rate Percent Differences for Heterogeneous, 2-D Case 54

Figure 32: DONJON (tr) Fission Rate Percent Difference for Heterogeneous 2-D Case... 54

Figure 33: X Mesh Convergence Study in DRAGON 65

Figure 34: Z-Mesh Convergence Study in DRAGON 66

LIST OF SYMBOLS

Symbol	Units	Meaning
$\boldsymbol{D_x}$	cm	Diffusion Coefficient
$\vec{\boldsymbol{J}}$	n/cm^2s^{-1}	Neutron Current. It is used for determining leakage of neutrons out of a given volume in the neutron transport equation.
$\boldsymbol{k_{eff}}$	-	k-effective. A multiplication constant in neutron transport and diffusion equations. When the number of neutrons produced are equal those lost, it is equal to one.
N	$nuclei/cm^3$	Number density of nuclei of an isotope in a given medium.
$\vec{\boldsymbol{r}}$	-	Position Vector (x, y, z)
$\boldsymbol{\rho}$	mk	Reactivity. It is related to the multiplication constant and is equal to zero when number of neutrons produced are equal to those lost.
$\boldsymbol{\Sigma_x}$	cm^{-1}	Macroscopic cross-section of a material, specific to reaction 'x'. Represents likelihood of neutron interaction.
$\boldsymbol{\sigma_x}$	cm^2	Microscopic cross-section of a nuclide, specific to reaction 'x'. Measured experimentally.
$\boldsymbol{\Phi}$	n/cm^2s^{-1}	Neutron Flux
$\boldsymbol{\Phi_1}$	n/cm^2s^{-1}	Fast Neutron Flux in 2 Energy Groups (E above 0.625 eV).
$\boldsymbol{\Phi_2}$	n/cm^2s^{-1}	Thermal Neutron Flux in 2 Energy Groups (E below 0.625 eV).
$\boldsymbol{\chi}$	-	Probability Distribution of Neutrons Born from Fissions as a function of Energy.

1. INTRODUCTION

1.1 CANDU Reactor Description

The CANDU[1®] reactor is a pressure-tube heavy-water moderated and cooled nuclear reactor (PT-HWR). The CANDU reactor, front view shown in Figure 1, has a large, cylindrical, horizontally-oriented calandria vessel. Within the calandria is low-pressure, low-temperature heavy-water moderator. The calandria also houses cylindrical fuel channels oriented axially and arranged in a square lattice configuration with a pitch of 28.575 cm.

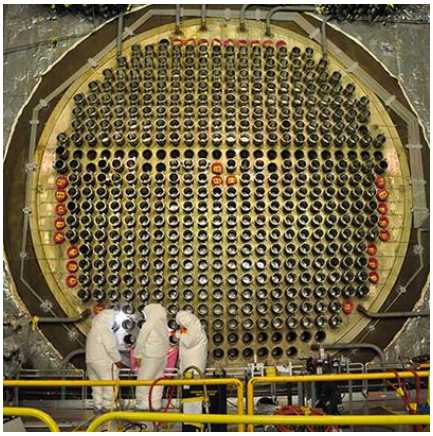

Figure 1: Pressure Tube Heavy Water Reactor *(Rosana, 2014)*

The fuel channel itself is made of a hollow zircalloy calandria tube, filled with carbon dioxide gas surrounding the pressure tube. High-pressure, high-temperature heavy water coolant flows through the zircalloy pressure tube and removes the heat generated by the twelve fuel bundles contained inside each pressure tube. Each fuel bundle has 37-elements. Each fuel element consists of a 48-cm stack of fuel pellets

[1] ® CANDU is a registered trademark of Atomic Energy of Canada Ltd. under license to Candu Energy Inc.

contained in a zircalloy-2 cladding. Fuel pellets are made of UO_2 with natural abundance of ^{235}U. A picture of the bundle can be seen in Figure 2.

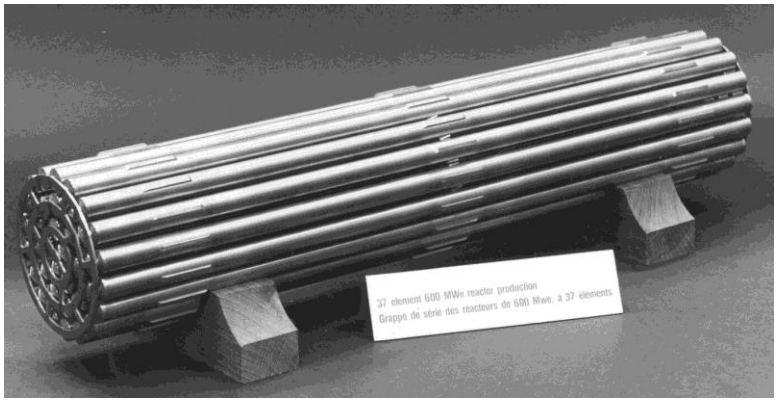

Figure 2: 37-Element Fuel Bundle *(Page, 2012)*

The pressure tube heavy water reactor analyzed in this study uses natural-uranium oxide (UO_2) fuel. Natural uranium consists of 99.289 wt% ^{238}Uuranium-, a fertile isotope, and 0.711 wt% ^{235}U, a fissile isotope. Under neutron irradiation, the fertile nuclide ^{238}U mutates into fissile nuclides such as ^{239}Pu and ^{241}Pu. Fissile nuclides have a high fission cross section for thermal neutrons. Consequently, natural-uranium fueled thermal reactors produce heat through fission reactions occurring in all fissile isotopes (e.g. ^{235}U, ^{239}Pu, ^{241}Pu). The fission reaction is initiated by a thermal neutron interacting with the nucleus and results in several high energy (or 'fast') neutrons being released, in addition to gamma rays, heat, and the splitting of the uranium nucleus into several lighter fission fragments. The fast neutrons produced during fission can move throughout the reactor and typically undergo many scattering reactions, especially when they reach the moderator region before being either absorbed or leaking out of the reactor. The energy of the fast neutrons is dispersed by scattering off of many nuclei, and causes them to become low energy or 'thermal' neutrons which are ready to initiate

a fission inside the fissile nuclides – thus propagating the chain reaction. The heat in the fuel is then carried away by the heavy water coolant to the steam generators, the steam produced in the steam generator is directed to a turbine which converts the heat into electrical energy. A heavy-water *reflector* surrounds the reactor to reduce neutron leakage from the reactor. This is done for two reasons: economically it is best to lose as few neutrons as possible to improve the amount of power extracted from the fuel and to prevent external reactor components from getting irradiated by the neutrons.

The process of irradiating nuclear fuel inside a power reactor changes the composition of that fuel either by the fission reaction (changing fissile material into several lighter mass fission products) or by absorption causing nuclei to change by adding a neutron and subsequently releasing a gamma ray (such as uranium-238 absorbing a neutron to become plutonium-239, a fissile isotope). This change in composition in the fuel in the field of reactor physics is referred to as the depletion or burnup of the fuel. Where burnup is defined as the amount of power produced by the fuel per unit mass of initial heavy elements, such as uranium, in the fuel. An example of fuel depletion occurring in natural uranium based fuel and some of the isotopic changes that occur are given in Figure 3.

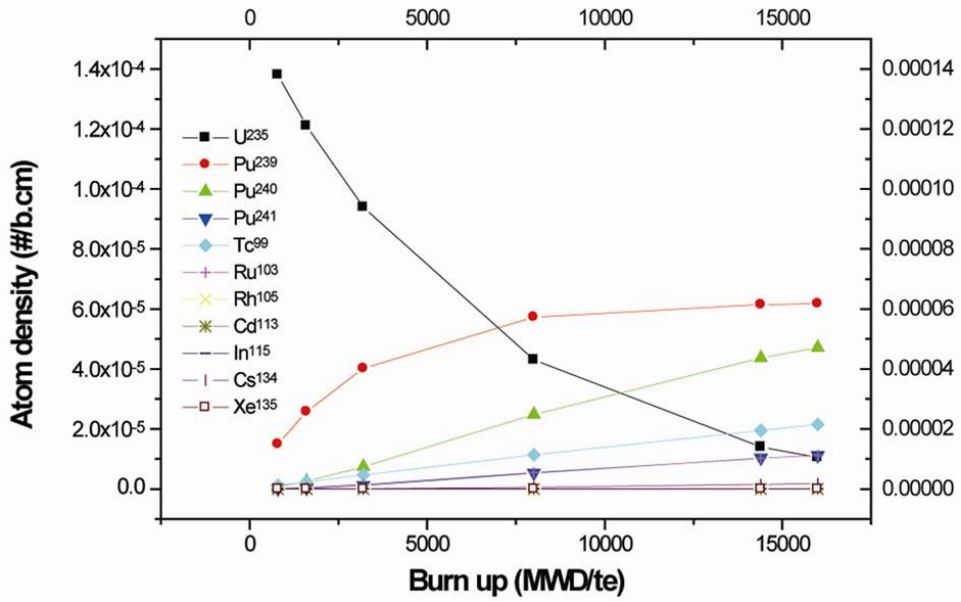

Figure 3: Atom Density in atoms/barn·cm of Important Isotopes as a function of Burn-up for Natural Uranium Fuel *(Yasin, Iqbal, & Shahzad, 2011)*

When predicting the behavior of such a complex system, there are multiple levels of analysis required, each looking at a different aspect of the core. Reactor physics analysis is primarily concerned with determining the distribution of the neutron flux, fission rate, and power density in the reactor core, as these pieces of information constitute the starting point for any thermal-hydraulic and safety-analysis calculation. The neutron flux can be described as the neutron density in a unit volume multiplied by the speed at which the neutrons are travelling. The flux can be determined by solving the neutron transport equation for a detailed representation of the core, including details such as the materials within the reactor and the temperature distribution.

1.2 Microscopic and Macroscopic Nuclear Cross-Sections

As mentioned in the introduction, the important part of modelling the physics of a nuclear reactor is determining the neutron flux by solving the neutron transport equation.

Nuclear data is used in the neutron transport equation to define source and loss terms. Nuclear data, in the form of microscopic cross sections, is a tabulated list of interaction probabilities for a neutron within any medium. The microscopic cross section, symbolized by σ, can be thought of as the cross-sectional area of a nucleus and has units of cm^2 or the more commonly used *barn* (1 barn = 10^{-24} cm^2) . Figure 4 shows the microscopic fission cross section for U-235 (the main fissile isotope used in natural uranium fueled PT-HWR's). This plot can be interpreted as the likelihood of a fission interaction for an incident neutron as a function of its energy. Therefore, a uranium-235 nucleus would have a much higher likelihood of causing a fission event for a lower energy neutron as opposed to a high-energy neutron. This is the reason why it is important to 'moderate' or slow-down the neutrons in a thermal nuclear reactor.

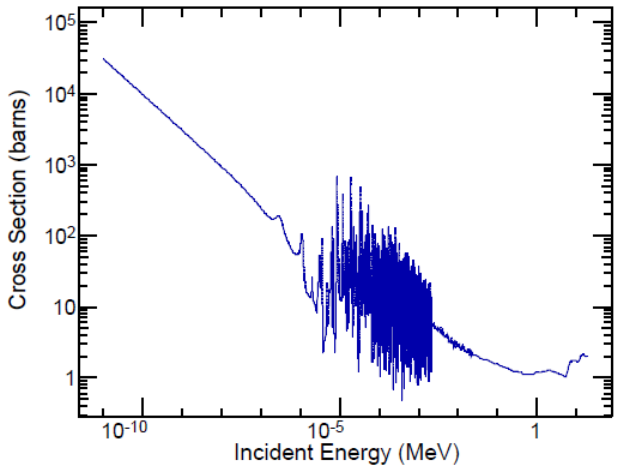

Figure 4: U-235 Fission Cross-Section *(Chadwick, 2011)*

Cross-sections are characterize single isotopes or elements. However, within a nuclear reactor the system is more complex and involves many elements mixed together to produce alloys or fuel. The way to capture these mixtures and to estimate

the overall effect is through the macroscopic cross-section (denoted as Σ). This quantity is defined in Equation 1:

$$\Sigma_R = \sum_{i=1}^{n} N^i \sigma_R^i \quad (1)$$

where R symbolizes the type of reaction that the cross section is characterizing, i is the index for the particular isotope, n is the total number of different atom species present in the material, and N^i is the number density (nuclei/cm^3) of a given isotope/element, i. The summation is performed over all isotopes in the material. The macroscopic cross section represents the probability of interaction per unit distance travelled by the neutron and its units are cm^{-1}.

The reactions a neutron can undergo while moving through a reactor are absorption and scattering. Fission is a particular type of absorption, whereby the compound nucleus formed through neutron absorption splits into (usually two) fission fragments and additional neutrons are emitted.

1.3 CANDU Modelling Summary

A lattice cell is defined in this work as a two-dimensional cross-section of a single CANDU fuel channel and surrounding moderator, with a lattice pitch of 28.575 cm in the x and y directions. An example of the lattice cell is depicted in Figure 5.

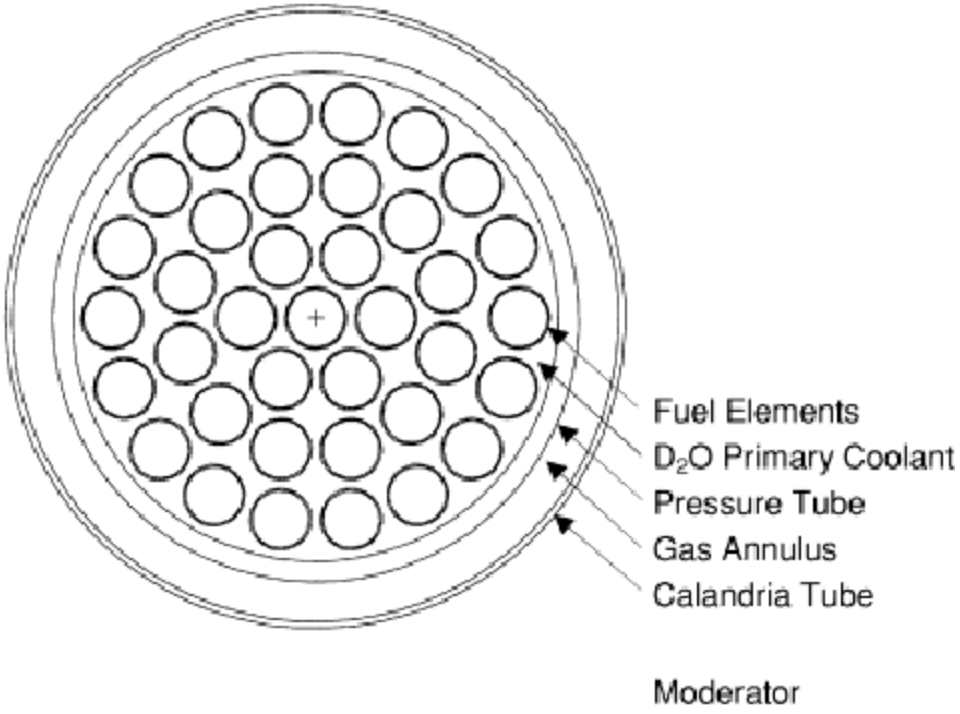

Figure 5: 37-Element CANDU Lattice Cell *(Hangbok, Gyuhong, & Donghwan, 2005)*

The first step of a full-core physics analysis involves solving the transport equation numerically for a single lattice cell to capture the fine spatial distribution of the flux inside the lattice cell and to generate flux-weighted averages of the macroscopic cross sections over the entire cell and over few (usually two) energy groups. Lattice calculations also include depletion calculations whereby the fuel composition as a function of burnup is determined. The burnup is defined as the energy liberated per initial mass of U. Cell-averaged macroscopic cross sections are calculated at several burnup steps. At each burnup step, cell-averaged cross sections are calculated for several values of "local" parameters such as fuel temperature, coolant temperature, coolant density, moderator temperature and mass density. The results of lattice and

burnup calculations are therefore summarized as tables which contain values of the cell-averaged macroscopic cross section as a function of burnup and local parameters.

Three-dimensional full-core calculations are subsequently performed using the diffusion approximation to the transport equation for a simplified model, whereby each lattice cell is represented as homogeneous. The corresponding macroscopic cross sections are found based on the bundle burnup and local parameters by interpolating in the tables previously generated by the lattice (and depletion) calculations.

1.4 Review of Homogenization Techniques

Numerous methods presently exist for condensing the multi-group transport equation (solved for an infinite lattice) into few energy group macroscopic cross sections and diffusion coefficients.

For CANDU type reactors, the industry standard lattice cell transport code used is WIMS-AECL (Altiparmakov D. V., 2008). A multicell correction method was prepared to capture the effect of leakage at the core-reflector interface (Altiparmakov & Shen, 2013). This method involves preparing a separate set of fuel macroscopic cross-section tables for the lattices bordering the reflector using multiple cells in lieu of single lattice cell calculations. The correction is applied to compensate for the discrepancies found between diffusion calculated bundle power distributions in the industry standard full-core neutron diffusion code RFSP (Rouben B. , 1995) in comparison to those found using the stochastic neutron transport code MCNP (Brown, 2002). An analogous model of multiple lattice cells is simulated for a given fuel burnup state, either a 1D model with a number of fuel lattice cells adjacent to a reflector cell or a corner interface (2x2) with a

single fuel lattice bordered by reflector cells. From multi-cell calculations, heterogeneous factors are calculated as a ratio between the single cell homogenized cross-sections and the multi-cell homogenized cross-sections and are then applied to the full core diffusion case where they are applicable (near the reflector). They are used to directly adjust the flux weighted homogenized two-group cross-sections. Similar improvements were achieved in bundle power predictions using the multi-cell method in comparison to those achieved using transport fitted diffusion coefficients with a reduction power errors in a 2D stylized full-core slice of an Advanced CANDU Reactor (ACR-1000[2®]) from 6% to less than 1%.

1.5 Research Motivation

The reason for using the diffusion approximation and homogenized cells is to reduce the computational expense. A single lattice cell transport calculation can take about two hours on one CPU. Solving the transport equation for a full-core, including 380 channels each with 12 bundles, and 37 fuel elements in each bundle with different local parameters would take more than one year and would require inordinately large memory resources

Generally, the diffusion approximation applied to a cell-homogenized core works well, except at the core-reflector interface. The curvature of the flux changes approaching the reflector, and this is inadequately captured when using two-group macroscopic cross-sections calculated using a single-cell model.

[2] ® ACR-1000 is a registered trademark of Atomic Energy of Canada Ltd. under license to Candu Energy Inc.

Several methods have been developed for handling the issues associated with the core-reflector interface. The multicell method relies on building fuel tables using multiple lattice cells representing the fuel and the reflector to obtain more realistic two-group macroscopic cross-sections. The industry standard neutron transport and diffusion codes WIMS-AECL (Altiparmakov D. V., 2008) and RFSP (Rouben B. , 1995) are modified to use the multicell method (Altiparmakov & Shen, 2013). Multicell tables improve predictions of flux calculations at the fuel-reflector boundary, but can be computationally intensive and add another layer of complexity to the analysis. Key concerns include managing multiple fuel tables and applying them in the correct locations.

A second, less computationally-intensive, method involves using transport-fitted diffusion coefficients. Patel (2010) has shown that for 1-D and 2-D cases it is possible to significantly improve the solution of the diffusion equation using this method. However, that method has not, to date, been applied to 3D cases or to cases involving coolant voiding, an important configuration for PT-HWRs.

Given the promising preliminary results obtained using the transport-fitted diffusion coefficients, it is important to study whether they can be just as successfully applied to cases including coolant voiding and to three-dimensional configurations.

1.1 Objective

The goal of the present work is to expand the previous work by Patel and examine the applicability of transport-fitted diffusion coefficients to three-dimensional configurations and to configurations including large perturbations in the local

parameters, such as the loss of coolant in the pressure tube. It aims to investigate if diffusion coefficients derived for a simple one dimensional case can be applied to more complex geometries as it is computationally challenging to create large, transport models to use for fitting the diffusion coefficients.

A secondary goal is to verify if prior results are reproducible using known diffusion codes within academia, namely the diffusion code DONJON (Varin, Hebert, Roy, & Koclas, 2005) as opposed to BlackStallion (Patel, 2010).

2. METHODS

2.1 The Neutron Transport Equation

To define a neutron's position and velocity six scalar parameters are used. Firstly, there is the position represented by the position vector $\vec{r} = (x, y, z)$. Secondly, there is the energy, which also defines the speed of the particle ($E = \frac{1}{2}mv^2$). Thirdly, there is the direction of the speed defined by $\vec{\Omega} = (\theta, \phi)$. The six scalar parameters define the phase space.

When integrating over the surface of a unit sphere (as the azimuthal and polar angles can define) the limits on the polar and azimuthal angles for defining the trajectory of the neutron are as follows: $0 \leq \theta \leq 2\pi$ for the azimuthal angle and $0 \leq \varphi \leq \pi$ for the polar angle.

The neutron angular density is denoted by $N(\vec{r}, \vec{\Omega}, E)$ and is defined as the expected number of neutrons in a small volume dV about a given position, moving in a solid angle dΩ about a given direction, and having the energy in a small interval dE about a specified energy, divided by the volume (dV), solid angle (dΩ), and energy(dE). Its typical unit is $cm^{-3}keV^{-1}$. While this density can be described as time dependent, $N(\vec{r}, \vec{\Omega}, E, t)$, the following derivation will focus on the steady state neutron transport equation (therefore removing the time dependency).

The angular neutron flux, given in Equation 2, is the product of the angular neutron distribution with the speed of the neutrons. Its typical unit is $cm^{-2}keV^{-1}s^{-1}$.

$$\Phi(\vec{r}, \vec{\Omega}, E) = vN(\vec{r}, \vec{\Omega}, E) \quad (2)$$

The transport equation represents the neutron balance equation for each infinitesimal phase-space volume, $dxdydzd\Omega dE$. For the static case the rate of neutron production equals the rate of neutron loss. The rate at which neutrons are produced has several source terms. First, there is the 'external source' term, which represents neutron sources independent of the flux level and is denoted by $S(\vec{r}, E)$. In what follows, it will be assumed that the external source is isotropic. External neutron sources would typically be used in sub-critical systems as a means of driving the chain reaction towards criticality.

The second source term is neutron fission – they key process at work in a nuclear reactor for producing power. It is expressed by:

$$\frac{\chi(E)}{4\pi} \int_{E'} \int_{\Omega'} \Phi\left(\vec{r}, \vec{\Omega}', E'\right) \nu\Sigma_f(\vec{r}, E')\, d\,\vec{\Omega}' dE' \tag{3}$$

χ(E) is the fission spectrum, that is the fraction of neutrons produced at a given energy due to a fission event. The 4π term is used to obtain the angular density, as the fission source is assumed isotropic. The most important term here is $\nu\Sigma_f(\vec{r}, E')$ which represents the macroscopic production cross section, which is the product between the macroscopic fission cross section, $\Sigma_f(\vec{r}, E')$ and the average number of neutrons emitted per fission, v. The fission macroscopic cross section has units of cm^{-1} and it represents the probability that a fission event will occur per unit distance travelled by the neutron; The number of neutrons produced per fission event depends on the incident-neutron energy, E, so the notation $\nu\Sigma_f(\vec{r}, E')$ is, in fact, an abbreviation for $\nu(E')\Sigma_f(\vec{r}, E')$. Note that the integral is taken over all energies and angles to find all of

the fissions occurring per unit angle and energy in the region and then the fission distribution factor determines the total number of neutrons produced due to fissions at the desired energy.

A third source term consists of neutrons with energies E' (different from E), travelling in direction Ω' which after colliding with a nucleus end up having an energy in the interval dE about E and travel along a direction comprised in dΩ about Ω. This scattering source term is expressed by:

$$\int_{E'} \int_{\Omega'} \Phi\left(\vec{r}, \vec{\Omega}', E'\right) \Sigma_s\left(\vec{r}, \vec{\Omega}' \to \vec{\Omega}, E' \to E\right) d\,\vec{\Omega}' dE' \tag{4}$$

The scattering-source term is not assumed to be isotropic, as angle is taken into consideration in the scattering cross section, defined as $\Sigma_s\left(\vec{r}, \vec{\Omega}' \to \vec{\Omega}, E' \to E\right)$. The integral takes into account every possible direction and energy a neutron could be scattered from to "push" it into the direction and energy of interest.

Next, the loss terms is considered. Firstly, there are losses due to absorptions in target nuclei, where the macroscopic absorption cross-section is represented by $\Sigma_a(\vec{r}, E)$. The absorption term is:

$$\Phi\left(\vec{r}, \vec{\Omega}, E\right) \Sigma_a(\vec{r}, E) \tag{5}$$

Secondly, neutrons can be lost through scattering interactions, where a neutron with the energy and direction of interest undergoes a scattering event and changes energy and direction. The scattering loss term is expressed as:

$$\Phi\left(\vec{r}, \vec{\Omega}, E\right) \Sigma_s(\vec{r}, E) \tag{6}$$

The total macroscopic scattering cross section, $\Sigma_s(\vec{r}, E)$ can be expressed as a function of the differential scattering cross section $\Sigma_s\left(\vec{r}, \vec{\Omega} \rightarrow \vec{\Omega}', E \rightarrow E'\right)$, as:

$$\Sigma_s(\vec{r}, E) = \int_{E'} \int_{\Omega'} \Sigma_s\left(\vec{r}, \vec{\Omega} \rightarrow \vec{\Omega}', E \rightarrow E'\right) d\,\vec{\Omega}' dE' \tag{7}$$

The integral takes into account every possible energy and direction that a neutron could be scattered to.

Lastly, neutrons can be lost through leakage. The leakage term represents the net rate at which neutrons exit the spatial infinitesimal volume of interest divided by that volume. A negative value implies that overall, there is a net influx of neutrons. The leakage rate is defined using the 'angular current', defined in Equation 8:

$$\vec{J}\left(\vec{r},\vec{\Omega},E\right)=\Phi\left(\vec{r},\vec{\Omega},E\right)\vec{\Omega} \tag{8}$$

The magnitude of the angular current is simply the angular flux, $\Phi\left(\vec{r},\vec{\Omega},E\right)$. The leakage term is defined as:

$$\lim_{V \rightarrow 0} \frac{1}{V} \int_S \vec{J}\left(\vec{r_s},\vec{\Omega},E\right) \cdot \vec{n}_s d\vec{S} \tag{9}$$

In this case, it is useful to review Gauss' Theorem.

$$\int_S \vec{J}\left(\vec{r_s},\vec{\Omega},E\right) \cdot \vec{n}_s d\vec{S} = \int_V \nabla \cdot \vec{J}\left(\vec{r_s},\vec{\Omega},E\right) dV \tag{10}$$

The net leakage loss term is then defined as:

$$\vec{\nabla} \cdot \vec{J}\left(\vec{r},\vec{\Omega},E\right) = \vec{\Omega} \cdot \nabla\, \Phi\left(\vec{r},\vec{\Omega},E\right) \tag{11}$$

The next step involves gathering together all of the source terms and loss terms into one equation (in this case, let us assume the system is at steady state and therefore losses equal sources).

$$\frac{S(\vec{r},E)}{4\pi}+\frac{\chi(E)}{4\pi}\int_{E'}\int_{\Omega'}\Phi(\vec{r},\vec{\Omega}',E')\nu\Sigma_f(\vec{r},E')\,d\,\vec{\Omega}'dE'+$$

$$\int_{E'}\int_{\Omega'}\Phi(\vec{r},\vec{\Omega}',E')\Sigma_s(\vec{r},\vec{\Omega}'\rightarrow\vec{\Omega},E'\rightarrow E)\,d\,\vec{\Omega}'dE'=$$

$$\overrightarrow{\Omega}\cdot\nabla\,\Phi(\vec{r},\overrightarrow{\Omega},E)+\Phi(\vec{r},\vec{\Omega},E)\Sigma_s(\vec{r},E)+\Phi(\vec{r},\vec{\Omega},E)\Sigma_a(\vec{r},E) \quad (12)$$

Another way of representing the out-scattering and absorption terms is by summing them into the total cross section. This will shorten the representation of the equation.

$$\Sigma_t(\vec{r},E)=\Sigma_s(\vec{r},E)+\Sigma_a(\vec{r},E) \quad (13)$$

Substituting this into the derived transport equation, the following form is obtained:

$$\frac{S(\vec{r},E)}{4\pi}+\frac{\chi(E)}{4\pi}\int_{E'}\int_{\Omega'}\Phi(\vec{r},\vec{\Omega}',E')\nu\Sigma_f(\vec{r},E')\,d\,\vec{\Omega}'dE'+$$

$$\int_{E'}\int_{\Omega'}\Phi(\vec{r},\vec{\Omega}',E')\Sigma_s(\vec{r},\vec{\Omega}'\rightarrow\vec{\Omega},E'\rightarrow E)\,d\,\vec{\Omega}'dE'=$$

$$\overrightarrow{\Omega}\cdot\nabla\,\Phi(\vec{r},\overrightarrow{\Omega},E)+\Phi(\vec{r},\vec{\Omega},E)\Sigma_t(\vec{r},E) \quad (14)$$

2.2 The Diffusion Approximation

The neutron transport equation is a challenging one to solve numerically as it depends on six independent variables and contains both energy and angle integrals and spatial derivatives (in the gradient term). For a full-core solution in a PT-HWR type

problem, the equation needs to be simplified to make it computationally feasible. The focus of this section is on moving from the transport equation to the two-group neutron diffusion equation.

First, it is important to integrate out the angular dependence from each term in the transport equation (thus removing two of the six variables). The most challenging component is the in-scattering term:

$$\int_{\Omega}\int_{E'}\int_{\Omega'} \Phi\left(\vec{r},\vec{\Omega}',E'\right)\Sigma_s\left(\vec{r},\vec{\Omega}'\rightarrow\vec{\Omega},E'\rightarrow E\right)d\vec{\Omega}'\,dE'\,d\vec{\Omega} \tag{15}$$

The scattering cross-section depends only on the cosine of the angle between $\vec{\Omega}'$ and$\vec{\Omega}$, μ=$\vec{\Omega}'\cdot\vec{\Omega}$, which renders the scattering term more manageable, especially since the scattering angle is independent of the azimuthal component.

$$=\int_{E'}\Phi(\vec{r},E')\int_{\mu}2\pi\Sigma_s(\vec{r},E'\rightarrow E,\mu)d\mu\,dE' \tag{16}$$

Note that the 2π term is obtained from integrating over the independent azimuthal angle. By using the cosine of the scattering angle in the expression of the scattering cross section:

$$\Sigma_s(\vec{r},E'\rightarrow E)=2\pi\int_{\mu}\Sigma_s(\vec{r},E'\rightarrow E,\mu)d\mu \tag{17}$$

a scattering term is obtained that is independent of the solid angle, Ω.

$$\int_{E'}\Phi(\vec{r},E')\Sigma_s(\vec{r},E'\rightarrow E)\,dE' \tag{18}$$

The next term is the leakage term.

$$\int_{\vec{\Omega}} \vec{\nabla} \cdot \vec{J}(\vec{r},\vec{\Omega},E)d\vec{\Omega} = \vec{\nabla} \cdot \vec{J}(\vec{r},E) \tag{19}$$

Moving on to the other terms, the source term, total loss term (absorption + out-scattering) and fission term are solved next and are a simple matter of integrating out the angular dependency.

$$\frac{1}{4\pi}\int_{\vec{\Omega}} S(\vec{r},E)d\vec{\Omega} = S(\vec{r},E) \tag{20}$$

$$\int_{\vec{\Omega}} \Phi(\vec{r},\vec{\Omega},E)\Sigma_t(\vec{r},E)\, d\vec{\Omega} = \Phi(\vec{r},E)\Sigma_t(\vec{r},E) \tag{21}$$

$$\frac{\chi(E)}{4\pi}\int_{\vec{\Omega}}\int_{E'} \Phi(\vec{r},E')\nu\Sigma_f(\vec{r},E')\, dE'\, d\vec{\Omega} = \chi(E)\int_{E'} \Phi(\vec{r},E')\nu\Sigma_f(\vec{r},E')\, dE' \tag{22}$$

Now, when equating losses with gains for the steady state equation we obtain:

$$S(\vec{r},E) + \chi(E)\int_{E'} \Phi(\vec{r},E')\nu\Sigma_f(\vec{r},E')\, dE' +$$
$$\int_{E'} \Phi(\vec{r},E')\Sigma_s(\vec{r},E' \to E)\, dE' = \Phi(\vec{r},E)\Sigma_t(\vec{r},E) + \vec{\nabla} \cdot \vec{J}(\vec{r},E) \tag{23}$$

The leakage term is still dependent on the direction, $\vec{\Omega}$, though the initial desire of integrating out the solid angle was to obtain an equation purely dependent on the integral flux. This is where the heart of the diffusion approximation is applied through Fick's Law. The main idea within Fick's Law is that the neutrons will move from an area of high neutron flux to an area of low neutron flux. The current describing such "flow" is proportional to the spatial derivative of the flux. In three dimensions, the current can therefore be approximated as described in Equation 24.

$$\vec{J}(\vec{r},E) = -D\nabla\Phi(\vec{r},E) \tag{24}$$

where D is the diffusion coefficient with units of centimeters and calculated as one third of the macroscopic transport cross section. The traditional unit of the diffusion coefficient in molecular diffusion is in cm^2s^{-1}.

$$D = \frac{1}{3\Sigma_{tr}} \tag{25}$$

The transport cross-section in an absorbing medium can be calculated as given in Equation 26, where $\bar{\mu}$ is the average of the cosine of the scattering angle and acts as a measure of how anisotropic the neutron scattering is.

$$\Sigma_{tr} = \Sigma_a - \Sigma_s(1 - \bar{\mu}) \tag{26}$$

The limitation of Fick's law is that it is only valid for linearly isotropic scattering in mediums without strong absorption and for cases that have flux values that do not vary strongly over short distances within the core. Now that all the terms have been simplified to a dependence on the integrated flux, they can be collected to form the diffusion equation.

$$S(\vec{r}, E) + \chi(E) \int_{E'} \Phi(\vec{r}, E')\nu\Sigma_f(\vec{r}, E')\, dE' + \int_{E'} \Phi(\vec{r}, E')\Sigma_s(\vec{r}, E' \to E)\, dE' = \Phi(\vec{r}, E)\Sigma_t(\vec{r}, E) - \vec{\nabla} \cdot D\nabla\Phi(\vec{r},\mathrm{E}) \tag{27}$$

2.3 The Two-Group Diffusion Equation

The diffusion equation derived above is continuously dependent on neutron energy. Alternatively, the energy domain can be divided into intervals called energy groups. Correspondingly, the group diffusion equation is obtained by integrating the continuous-energy equation over each energy group. In this work, the two-energy

group neutron diffusion equation is employed to solve for the flux. The first energy group extends form 0.625 eV to 10 MeV and is used to represent epithermal and fast neutrons. The second energy group extends from 0 eV to 0.625 eV and is used to represent thermal neutrons. Some terms of the two-group diffusion equations are derived below.

$$E_0 = 10\ MeV, E_1 = 0.625\ eV, E_2 = 0\ eV \tag{28}$$

$$\phi_g = \int_{E_g}^{E_{g-1}} \phi(E)dE, \qquad g = 1,2 \tag{29}$$

$$\Sigma_{ag} = \int_{E_g}^{E_{g-1}} \phi(E)\Sigma_a(E)dE, \qquad g = 1,2 \tag{30}$$

$$\chi_g = \int_{E_g}^{E_{g-1}} \chi(E)dE, \qquad g = 1,2 \tag{31}$$

$$\Sigma_{s_{1\to2}} = \frac{\int_{E_2}^{E_1}\int_{E_1'}^{E_0'} \phi(\vec{r},E')\Sigma_s(\vec{r},E'\to E)\,dE'dE}{\phi_1} \tag{32}$$

$$\Sigma_{s_{2\to1}} = \frac{\int_{E_1}^{E_0}\int_{E_2'}^{E_1'} \phi(\vec{r},E')\Sigma_s(\vec{r},E'\to E)\,dE'dE}{\phi_2} \tag{33}$$

$$\Sigma_{r1} = \Sigma_{a1} + \Sigma_{s\,1\to2} \tag{34}$$

$$\Sigma_{r2} = \Sigma_{a2} + \Sigma_{s\,2\to1} \tag{35}$$

The resulting two-group diffusion equation is:

$$\chi_1\left(\Phi_1(\vec{r})\nu\Sigma_{f_1}(\vec{r}) + \Phi_2(\vec{r})\nu\Sigma_{f_2}(\vec{r})\right) + \Phi_2(\vec{r})\Sigma_{s_{2\to1}}(\vec{r}) = \Phi_1(\vec{r})\Sigma_{r_1}(\vec{r}) - \vec{\nabla}\cdot D_1\nabla\Phi_1(\vec{r}) \tag{36}$$

$$\chi_2\left(\Phi_1(\vec{r})\nu\Sigma_{f_1}(\vec{r}) + \Phi_2(\vec{r})\nu\Sigma_{f_2}(\vec{r})\right) + \Phi_1(\vec{r})\Sigma_{s_{1\to2}}(\vec{r}) = \Phi_2(\vec{r})\Sigma_{r_2}(\vec{r}) - \vec{\nabla}\cdot D_2\nabla\Phi_1(\vec{r}) \quad (37)$$

In the above equations, a solution is only possible if the reactor is exactly critical (production = loss). However, it is of interest to know how far away from a critical state a system is, and therefore a factor is introduced to allow this equation to hold in non-critical configurations. The factor is termed the effective multiplication constant and is denoted by k_{eff}. It is used to adjust the fission source term.

$$\frac{\chi_1}{k_{eff}}\left(\Phi_1(\vec{r})\nu\Sigma_{f_1}(\vec{r}) + \Phi_2(\vec{r})\nu\Sigma_{f_2}(\vec{r})\right) + \Phi_2(\vec{r})\Sigma_{s_{2\to1}}(\vec{r}) = \Phi_1(\vec{r})\Sigma_{r_1}(\vec{r}) - \vec{\nabla}\cdot D_1\nabla\Phi_1(\vec{r}) \quad (38)$$

$$\frac{\chi_2}{k_{eff}}\left(\Phi_1(\vec{r})\nu\Sigma_{f_1}(\vec{r}) + \Phi_2(\vec{r})\nu\Sigma_{f_2}(\vec{r})\right) + \Phi_1(\vec{r})\Sigma_{s_{1\to2}}(\vec{r}) = \Phi_2(\vec{r})\Sigma_{r_2}(\vec{r}) - \vec{\nabla}\cdot D_2\nabla\Phi_1(\vec{r}) \quad (39)$$

2.4 Deriving the Diffusion Coefficients from the Transport Solution

The premise of the present work is to take the two group diffusion equation as derived above and isolate for the diffusion coefficients and then calculate their value based on the transport solution of the flux in a simplified, but analogous system to the one of interest. The first step is to isolate for the diffusion coefficients in each energy group from the two-group diffusion equation. Note that in the formulas below the flux values are based on the transport flux, and the k_{eff} value is the transport evaluated k_{eff}.

$$D_1(\vec{r}) = \frac{\Phi_1(\vec{r})\Sigma_{r_1}(\vec{r}) - \Phi_2(\vec{r})\Sigma_{s_{2\to1}}(\vec{r}) - \frac{\chi_1}{k_{eff}}\left(\Phi_1(\vec{r})\nu\Sigma_{f_1}(\vec{r}) + \Phi_2(\vec{r})\nu\Sigma_{f_2}(\vec{r})\right)}{\nabla^2\Phi_1(\vec{r})} \quad (40)$$

$$D_2(\vec{r}) = \frac{\Phi_2(\vec{r})\Sigma_{r_2}(\vec{r}) - \Phi_1(\vec{r})\Sigma_{s_{1\to 2}}(\vec{r}) - \frac{\chi_2}{k_{eff}}\left(\Phi_1(\vec{r})\nu\Sigma_{f_1}(\vec{r}) + \Phi_2(\vec{r})\nu\Sigma_{f_2}(\vec{r})\right)}{\nabla^2\Phi_1(\vec{r})} \quad (41)$$

The finite difference method is used to approximate the Laplacian in the flux in the denominator of Equations 40 and 41. A two-dimensional example is discussed here.

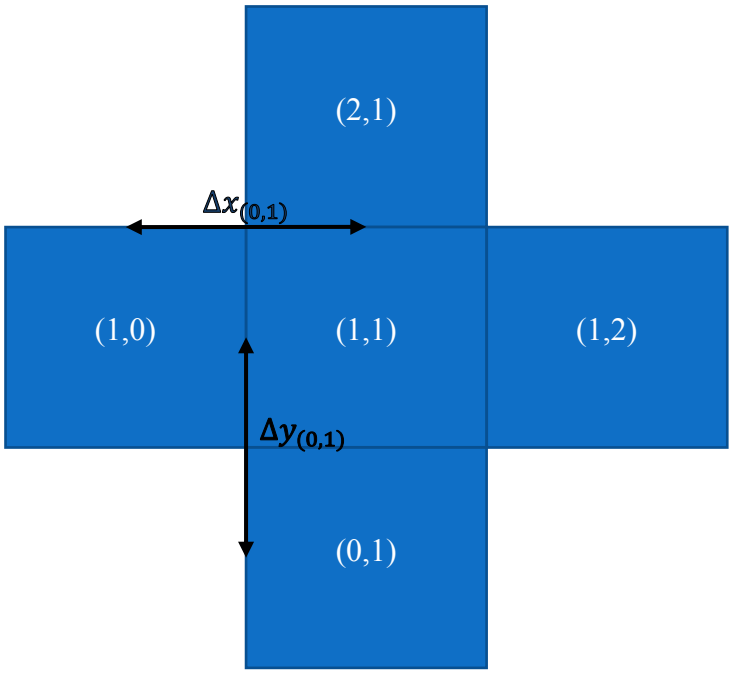

Figure 6: Example Elements for Estimating Flux Laplacian

An example geometry is given in Figure 6, with four elements all bordering the central point at (1,1). The transport flux values are known at the center of each of these points. The method for estimating the flux gradient at point (1,1) will now be evaluated.

$$\nabla^2\phi_{(1,1)} = \frac{\partial^2\phi_{(1,1)}}{\partial x^2} + \frac{\partial^2\phi_{(1,1)}}{\partial y^2} \quad (42)$$

The second partial derivatives of the flux can be approximated using finite differences. As it may happen that adjacent nodes are of different dimension (or the meshes are non-uniform in size) the flux calculations are adjusted to accommodate for this potential by having separate variables for mesh sizes.

$$\nabla^2\Phi_{(1,1)} = \frac{\phi_{(1,0)} - 2\phi_{(1,1)} + \phi_{(1,2)}}{\Delta x_{(0,1)}\Delta x_{(1,2)}} + \frac{\phi_{(2,1)} - 2\phi_{(1,1)} + \phi_{(0,1)}}{\Delta y_{(0,1)}\Delta y_{(1,2)}} \quad (43)$$

The next step is to account for the nodes on a boundary. In this work the boundary conditions for the problem of interest are either reflective or vacuum. Figure 7 represents a system with reflective boundary conditions in the x direction at the boundary between node (0,1) and node (1,1). Meaning the flux at these two nodes would be equal. An approximation of the Laplacian for this case is now derived.

$$\nabla^2\Phi_{(1,1)} = \frac{-\phi_{(1,1)} + \phi_{(1,2)}}{\Delta x_{(0,1)}\Delta x_{(1,2)}} + \frac{\phi_{(2,1)} - 2\phi_{(1,1)} + \phi_{(0,1)}}{\Delta y_{(0,1)}\Delta y_{(1,2)}} \quad (44)$$

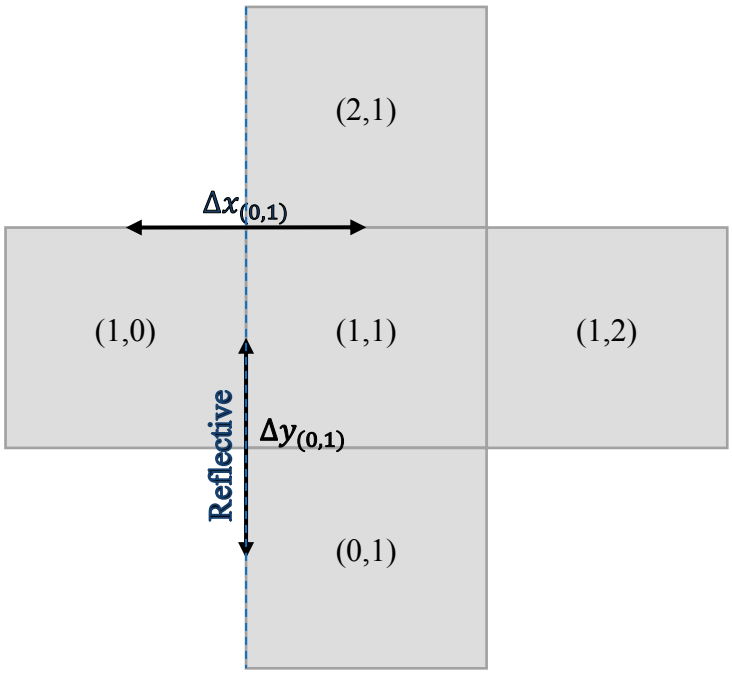

Figure 7: Example Elements for Estimating Flux Laplacian at Reflective Boundary

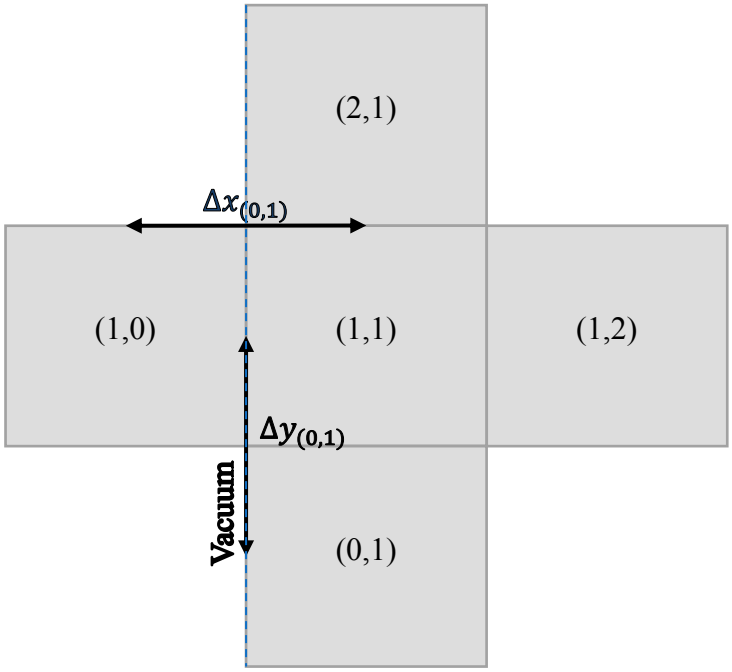

Figure 8: Example Elements for Estimating Flux Laplacian at Vacuum Boundary

Figure 8 shows an example for the vacuum boundary condition, it is assumed that the Flux at the midpoint between (1,0) and (1,1) has a zero value.

$$\nabla^2 \Phi_{(1,1)} = \frac{0 - 2\phi_{(1,1)} + \phi_{(1,2)}}{\frac{\Delta x_{(0,1)}}{2} \Delta x_{(1,2)}} + \frac{\phi_{(2,1)} - 2\phi_{(1,1)} + \phi_{(0,1)}}{\Delta y_{(0,1)} \Delta y_{(1,2)}} \tag{45}$$

$$\nabla^2 \Phi_{(1,1)} = \frac{-4\phi_{(1,1)} + 2\phi_{(1,2)}}{\Delta x_{(0,1)} \Delta x_{(1,2)}} + \frac{\phi_{(2,1)} - 2\phi_{(1,1)} + \phi_{(0,1)}}{\Delta y_{(0,1)} \Delta y_{(1,2)}} \tag{46}$$

2.5 Description of Nuclear Data and Codes Used

2.5.1 DRAGON

DRAGON is a scientific simulation code that can be used to solve the neutron transport equation by the collision probabilities method (Marleau, Herbert, & Roy, 2013). In this case the nuclear data library used is the 69 energy group ENDF/B-VII.0

WIMS-D format nuclear data library IAEALIB (WIMS Library Update, 2016). In this work, DRAGON is used in two ways. First it is used to solve a depletion calculation, whereby the composition of the fuel is calculated and then condensed into two energy group macroscopic cross-sections for later use in multiple cell problems. Second, it is used to simulate larger multiple cell problems and taken as the more accurate solution against which to compare DONJON (diffusion based) results to see if fitting the diffusion coefficients to the transport solution indeed improves the results. The first homogeneous, one dimensional multiple cell DRAGON model is used to transport fit the diffusion coefficients which are then used for the remaining diffusion analyses performed.

2.5.2 DONJON

DONJON is a scientific simulation code that can be used to solve the diffusion approximation of the neutron transport equation using the finite differences or the finite element method (Varin, Hebert, Roy, & Koclas, 2005). In this work, DONJON is used to model the larger multicell cases and compare against DRAGON. For every large geometry model studied, there are two DONJON models prepared. One DONJON model will exclusively use the homogenized cross-sections as prepared by DRAGON in the depletion calculations and the second DONJON model will use mostly the same nuclear data as the first model except for the transport cross-sections which are replaced with the transport fitted diffusion coefficient results obtained for the simplest one dimensional case studied (recall the relationship between the transport cross-section

and diffusion coefficient in Equation 25). An overview of the flow of data for the analysis that is performed here is provided in Figure 9.

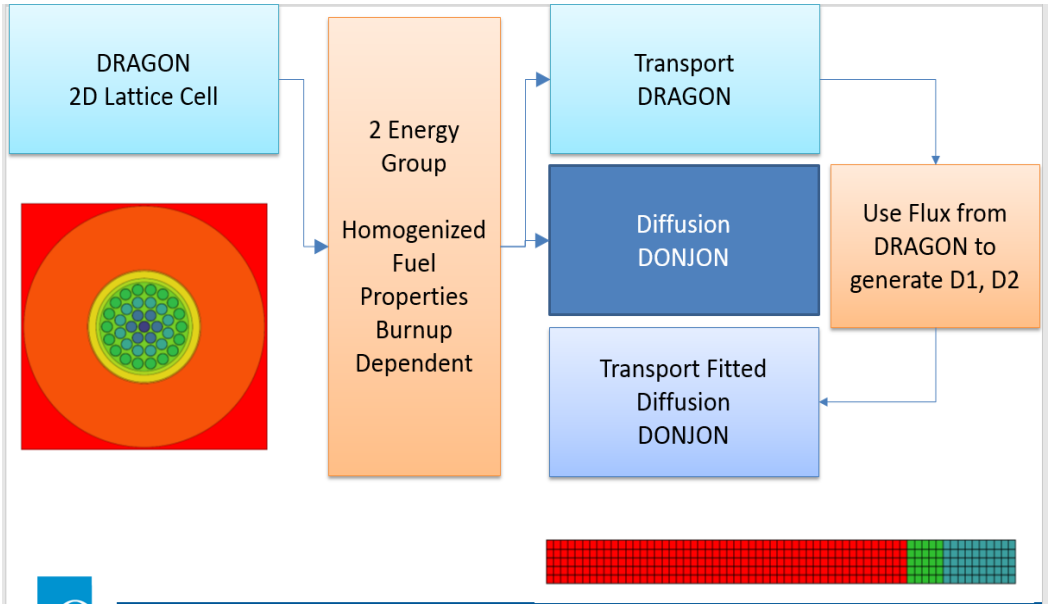

Figure 9: Data Flow of Physics Analysis Performed

2.6 Description of Physics Models Prepared

2.6.1 Lattice Physics Models

The geometry and material parameters used for performing the lattice physics depletion calculations are given in Table 1 and Table 2.

Table 1: Lattice Cell Geometric Parameters for Nominal and Cartesian Geometries

Parameter	Nominal Dimension	Cartesian Dimension (Length)	Units
Lattice Pitch	28.575	28.575	cm
Calandria Tube OR	6.587	11.657	cm
Calandria Tube IR	6.448	11.461	cm
Pressure Tube OR	5.603	9.972	cm
Pressure Tube IR	5.169	9.208	cm
Fuel Element OR	0.654	N/A	cm
Fuel Pellet OR	0.612	1.092	cm

A PT-HWR lattice cell contains a cylindrical calandria tube, pressure tube and fuel pins arranged in a cluster bundle formation (see Figure 2). The geometry is converted into a Cartesian form to make it possible to explicitly model the same geometry in DONJON, both the cluster and Cartesian geometries are presented in Figure 10. Though this was not done here, it is possible to evaluate pin powers in this Cartesian geometry in future work, if desired. The conversion between geometries was done to preserve first and foremost the fuel volume, second to preserve the total volume of moderator, and third to maintain the volume of the coolant and pressure tube. The main volume that provided flexibility in this conversion is the carbon dioxide gas gap, which was adjusted to preserve the remaining volume constraints.

Table 2: Lattice Temperature and Density Parameters

Parameter	Value	Units
Coolant Temperature	549	K
Fuel Temperature	1155	K
Clad Temperature	549	K
Moderator Temperature	346	K
Coolant Density	0.8366	grams/cm^3
Fuel Density	10.6	grams/cm^3
Moderator Density	1.0827	grams/cm^3
Pressure Tube Density	6.5	grams/cm^3
Calandria Tube Density	6.5	grams/cm^3
Fuel Composition	Natural Uranium Dioxide	-
Pressure Tube Composition	100% Zr	-
Calandria Tube Composition	100% Zr	-
Coolant Purity	99.75	at% D2O in H2O
Moderator Purity	99.91	at% D2O in H2O
Relative Power	31.97	Watts per gram
Fresh Burnup	0	MWd/TIHE
Mid Burnup	4400	MWd/TIHE
Exit Burnup	7600	MWd/TIHE

Due to the complexity of a fine mesh Cartesian model, the fuel sheath was omitted to reduce the number of regions and thus allow the performance of multiple-cell calculations without reaching the limits on available memory.

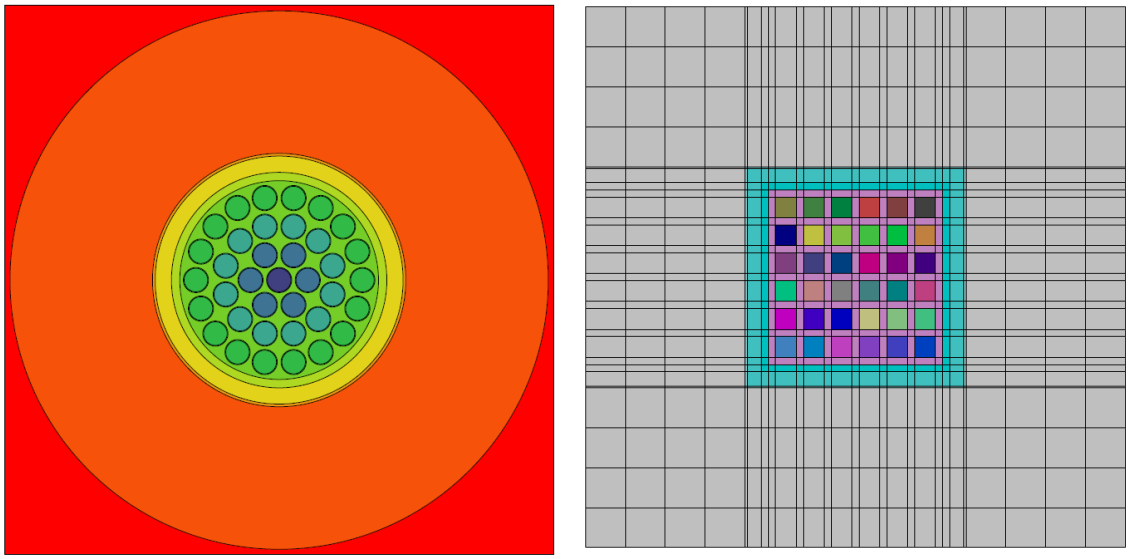

Figure 10: Lattice Cell Cluster Geometry (left) and Cartesian Geometry (right)

The first step in the lattice cell depletion analysis is to generate the necessary macroscopic cross-section data using a lattice cell transport calculation. This lattice analysis is carried out in the neutron transport code DRAGON (version 3.04) (Marleau, Herbert, & Roy, 2013) using the 69-energy group ENDF/B-VII.0 WIMS-D format nuclear data library IAEALIB (WIMS Library Update, 2016).

A depletion calculation is performed to determine fresh, mid-burnup and exit burnup fuel compositions for a natural uranium lattice cell. The depletion calculation has several steps. First, the library of mixtures is defined based on mixture densities and weight percentages of individual isotopes in each region within the lattice cell.

The geometry of the lattice cell is defined with reflective boundary conditions on all sides, each region in the geometry is assigned a mixture from the previously-defined library of mixtures and based on the composition data given in Table 2. Reflective boundary conditions mean that the model simulates an infinite array of the same lattice cell at the cell boundary, while a vacuum boundary condition means that if a neutron

passes through that boundary it is lost and cannot re-enter the simulation; in other words, the model has zero incoming neutron current on that boundary. Then a tracking calculation is performed, it is used to evaluate volumes, surface areas and define the tracking line locations within the geometry based on user input parameters (a user can input the density of tracking lines and different methods of integrating them). These tracking lines are used to discretize individual regions for the collision probability and flux calculation; it's important to have enough tracking line density or the accuracy of the solution may be impacted.

The collision probability matrices are then computed; they represent the probabilities of neutrons born in one region to interact in another region and depend on the energy group. Lastly, the flux is evaluated based on the collision probabilities for the defined geometry. Once the flux is evaluated for the problem, the fuel is 'depleted' or 'burned up' based on exposing the fuel to the evaluated flux values at a set bundle-power level (600 kW in this case) for a specified time interval. The composition of fuel is updated based on fuel depletion chains and fission product probability distributions. After this calculation is complete and another iteration of the above steps can be performed (except for library and geometry definitions). The lattice depletion calculation is complete when the desired number of time steps have been run.

The macroscopic cross-sections are homogenized by performing a two-energy group condensation and a full geometry homogenization. Homogenization occurs after each flux calculation and its results are written to an output file. The macroscopic cross sections are homogenized into two energy groups from 69 energy groups based on a

0.625 eV cut-off value. The reason two energy group are used (fast, group = 1, above 0.625 eV and thermal, group = 2, below 0.625 eV) is because in thermal reactors (such as PT-HWR) a large majority of fissions are induced by thermal neutrons (below 0.625 eV) and the fission rate is the most important to calculate correctly as it determines the power and heat generation rate. Capturing the thermal fission rate is considered accurate enough when performing diffusion calculations for CANDU type reactors (Rouben & Nichita, 2016).

The homogenization performed for an energy condensation of the cross-sections is flux weighted as shown in Equation 48 below.

$$\Sigma_{x,E_g}(r) = \frac{\sum_{E \epsilon E_g} \Sigma_x(r,E)\Phi(r,E)}{\sum_{E \epsilon E_g} \Phi(r,E)} \tag{48}$$

The cross-sections require an energy condensation to two groups and a full volume homogenization into a single region. This volume and flux average homogenization method is given in Equation 49, using the energy collapsed cross-sections.

$$\Sigma_{x,E_g} = \frac{\sum_{r \epsilon V} V(r)\Phi_{E_g}(r)\Sigma_{x,E_g}(r)}{\sum_{r \epsilon V} V(r)\,\Phi_{E_g}(r)} \tag{49}$$

2.6.1 Multicell Models

Three 1-D multicell cases, one 2-D and one 3-D case are used in this study, all listed in Table 3. For every geometry case, there are three different code results that are obtained. Namely, there is one DRAGON model prepared, and two DONJON models (data flow is depicted in Figure 9). The first DONJON model and the multicell DRAGON

model use the homogenized and condensed two energy group cross-sections obtained in the above described lattice depletion calculation. The second DONJON model uses this same two group library except for the diffusion coefficients which are replaced with the corrected diffusion coefficients obtained from the first (and only the first) homogeneous, 1-D case.

Table 3: Multicell Cases to be Modelled

Case	Void Surface	Fuel Area	Fuel/Void Ratio	Fuel Cells	Reflector Cells
1-D Homogeneous	28.575 cm	8981 cm^2	314	11	0
1-D Homogeneous, Void	28.575 cm	8981 cm^2	314	11	0
1-D Heterogeneous	28.575 cm	8981 cm^2	314	11	2
2-D Heterogeneous	742.95 cm	98,454 cm^2	132	121	48
3-D Heterogeneous	32,754 cm^2	161,205 cm^3	4.9	8	19

The three one-dimensional cases consist of the diffusion coefficient derivation case (1-D homogeneous) which is made up of 11 mid-burnup cells, the voided 1-D homogeneous case which is also made up of 11 mid-burnup cells but they are modelled with voided coolant (coolant density = 0.001 g/cm^3) and the heterogeneous 1-D case which is made up of 10 exit burnup fuel cells, 1 fresh fuel cell and two reflector cells. The reasoning behind choosing these three cases will now be described. The homogeneous 1-D case is used to derive the diffusion coefficients as it is assumed to be the approximate average fuel composition state of a real full-core model and may then best represent the system to be modelled. Then a state change is made with this same model geometry/composition to evaluate how well the derived diffusion coefficients for this ‘average’ model apply when parameters such as the coolant density are perturbed.

The heterogeneous model is used as a test of the limitations of the transport fitted diffusion coefficient since the fresh fuel is placed close to the vacuum boundary where the most leakage occurs. The 2-D case is an extension of this heterogeneous 1-D model but more leakage surface is introduced relative to the volume of fuel modelled (see the fuel/void ratio in Table 3).

The geometrical configuration of the one-dimensional homogeneous problem used to fit the diffusion coefficient to an analogous PT-HWR type configuration is a set of eleven mid-burnup lattice cells meant to represent half of a middle row of a typical 380 channel pressure tube heavy water reactor, as seen bordered in red in Figure 11. These eleven cells are adjacent to a reflector region, but as a simplifying measure, the reflector was not used for the diffusion coefficient derivation models. The 1-D model geometry is pictured in Figure 12. The boundary conditions in the 1-D case are reflective on all sides with exception of the core edge which has a vacuum boundary condition applied to mirror the impact of neutron leakage from the core (no re-entrant neutrons, inward current set equal to zero). Each lattice cell is divided into a five by five mesh when performing the DRAGON transport calculation to obtain more refined flux results.

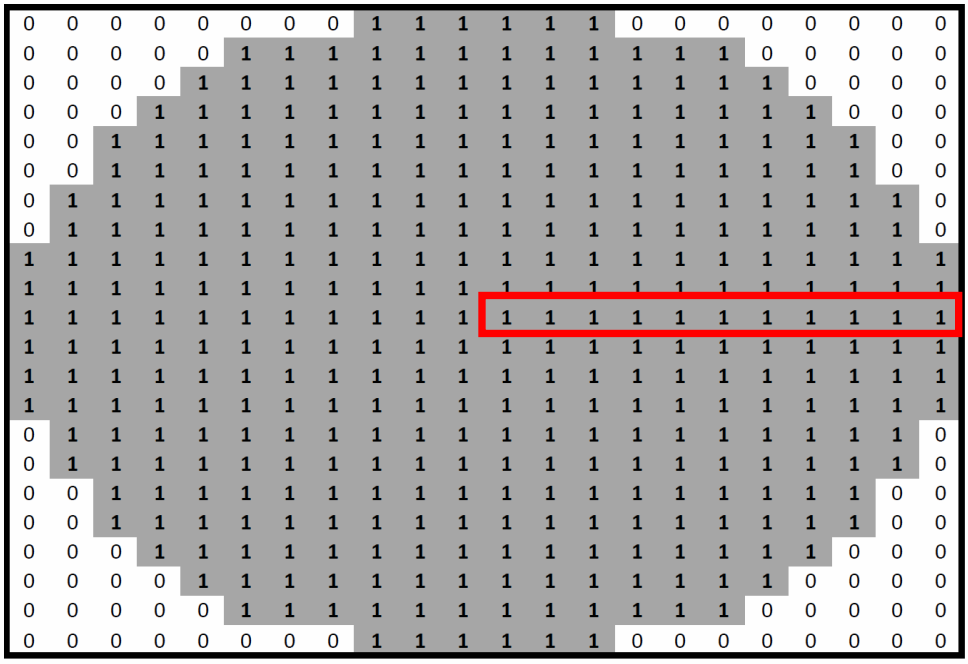

Figure 11: Reactor Face Layout

Figure 12: 1-D Homogeneous Case Geometry

Two energy groups are chosen here as the preferred energy group structure for the transport/diffusion multicell cases for three reasons. The first is ease of implementation. The second is to provide a true comparison with analogous cross sections in diffusion. The third reason was that it was previously proven (Patel, 2010) that two group homogenized transport demonstrates very similar cell averaged fluxes/fission rates to 69 group heterogeneous transport for CANDU type lattices.

The homogeneous 1-D case as described above is then modelled with a state change by setting the coolant density to 0.001 g/cm^3 in all the fuel-containing cells. In this case, the same lattice depletion model was run as described earlier with adjustments made at each depletion step to void the coolant and homogenize the cross-sections. Coolant voiding is an important phenomenon in the physics of CANDU type reactors, as it causes a positive reactivity change, which can lead to power increases.

This heterogeneous 1-D case is meant to test the burnup sensitivity of the derived diffusion coefficients. As they are found for a configuration with uniform, mid-burnup, fuel composition, it is worthwhile to test if they also work for different burnup values where the flux shape will significantly differ. The chosen case consists of ten exit-burnup fuel bundles, adjacent to one fresh fuel bundle which is bordered by two reflector cells (as depicted in Figure 13).

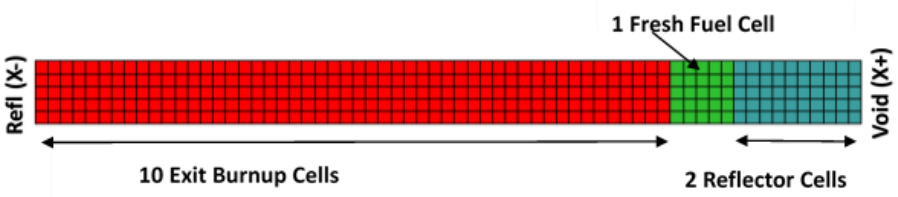

Figure 13: 1-D Heterogeneous Case Geometry

This model has reflective boundary conditions on all sides except for the positive x-axis boundary, where a vacuum boundary condition is used. The reasoning behind putting fresh fuel at the boundary is to impose an extreme variation in flux near the vacuum boundary which is a strong test of the diffusion approximations' limits.

The geometry studied in two-dimensions is an extension of the previously studied heterogeneous one-dimensional model. It is comprised of 10 x 10 exit burnup lattice cells bounded by one fresh fuel cell and two reflector cells on the right-most and bottom boundaries (see Figure 14). Vacuum boundary conditions are applied to the two edges of the model which are lined with reflector cells while the remaining fuel containing edges has reflective boundary conditions applied.

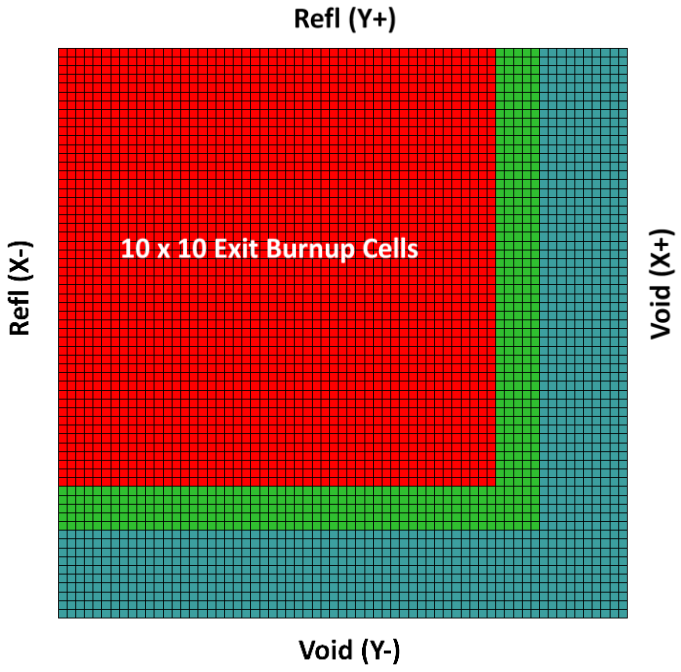

Figure 14: 2-D Heterogeneous Case Geometry

When moving from 1-D to 2-D calculations, applying the same diffusion coefficient works well as the lattice geometry is the same in the x and y directions, namely the lattice cells are square. The challenge is moving into a 3-D case while still maintaining the improvements achieved in the 2-D cases. A mesh convergence study is performed to ensure that further mesh refinement does not significantly impact the results. A study of the mesh-size impact is described in more detail in Appendix A. It is

found that the mesh size needs to be ~5cm, a size similar to that used in earlier studies. If the meshes are larger, they are not accurately capturing the physics of the problem and this error will impact results when moving to 3-D calculations. Unfortunately, using finer meshes limits the size of the problem that can be studied in 3-D because on upper limits in DRAGON memory allocation. The largest possible case that could accommodate the system with this mesh size and the same tracking line density is chosen: a 3x3x3 bundle model. Such a small model does have a benefit, in that it tests in an extreme manner the efficacy of transport-fitted diffusion coefficients at capturing strong leakage effects. The model size allowed for a similar configuration to the heterogeneous 2D model, seen stylized and not to scale in Figure 15 with a single exit burnup fuel bundle, surrounded on three sides by fresh fuel. The fresh fuel bundles are bounded by reflector (consisting of heavy water). On the faces with reflector bounding the model, vacuum boundary conditions are used and reflective boundary conditions are applied on all other faces.

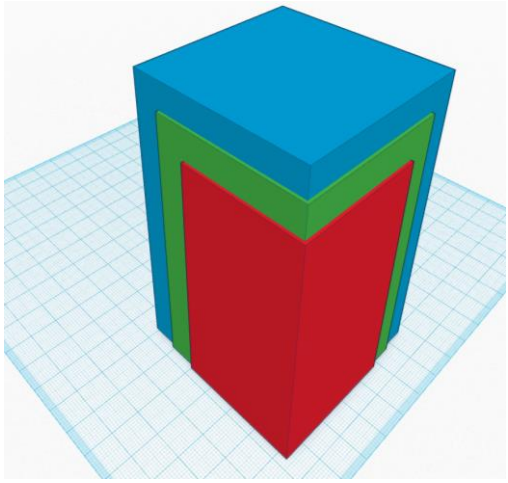

Figure 15: 3-D Heterogeneous Case Geometry
(Exit Burnup Fuel = Red, Fresh Fuel = Green, Reflector = Blue)

2.6.2 Evaluation Metrics for Multicell Cases

This work is concerned with reducing the error introduced by the use of the diffusion equation instead of the transport equation. Consequently, the transport-equation results provided by the DRAGON code are used as a reference against which the corresponding diffusion-equation results provided by the DONJON code are compared. All percent differences and Root Mean Square (RMS) errors evaluated in this work are evaluated against the respective DRAGON results. All fluxes, regardless of the code used to calculate them, are first normalized to a total fission rate of 1 fission/cm^3s^{-1}. The fission reaction rates per region are found using Equation 50 and the total fission rate for the entire geometry is determined using Equation 51.

$$RR_{fission}(r) = \left(\Phi_1(r)\Sigma_{f1}(r) + \Phi_2(r)\Sigma_{f2}(r)\right) \tag{50}$$

$$RR_{Tot_{Fission}} = \frac{\sum_{r\epsilon Geo} RR_{fission}(r)V(r)}{\sum_{r\epsilon Geo} V(r)} \tag{51}$$

The cell-averaged fission rate, fast flux and thermal flux calculated using the two approximate methods (DONJON code) are compared to the reference (DRAGON) results. Corresponding percent differences are evaluated using Equation 52.

$$\%\, Difference = \left(\frac{\phi_{DONJON} - \phi_{DRAGON}}{\phi_{DRAGON}}\right) 100\% \tag{52}$$

The RMS error is calculated according to Equation 53.

$$RMS\ Error = 100\% \sqrt{\frac{\sum_{x=1}^{N_{cells}} \left(\frac{\Phi_{DONJON}(x)}{\Phi_{DRAGON}(x)} - 1\right)^2}{N_{cells}}} \tag{53}$$

3. RESULTS

A homogeneous, one-dimensional, multicell DRAGON calculation is performed specifically to derive the transport fitted diffusion coefficients. A heterogeneous and voided homogeneous case are then prepared to test the effectiveness of the derived coefficients prior to moving on to more complex geometries.

3.1 Homogeneous, One-Dimensional, Diffusion-Coefficient-Derivation Case

The gradient of the fluxes obtained is evaluated at each region as described in the Methods section. The flux values, along with the two-group macroscopic cross sections are used to evaluate the two-group diffusion coefficients based on Equations 40 and 41. The coefficients are calculated on a fine mesh by mesh basis and then averaged to obtain one value for each energy group that are used in this study and applied over the entire geometry. The differences in these coefficients as a function of the x direction are shown in Figure 16. The vacuum boundary condition on the rightmost side introduces some instability into the gradient term, and therefore the values of D past the 200 cm mark are not included in the average. Figure 16 provides some insight into the behavior of diffusion coefficients in a system with defined leakage at the boundary, namely that the diffusion coefficients do not appear to significantly vary in space (aside from the instability near the vacuum boundary). Additionally, we see here that the derived coefficients are significantly higher than those which are calculated for the lattice cell in the DRAGON depletion calculation used to generate the macroscopic cross-sections. Having higher diffusion coefficients means that the region-to-region leakage will be proportionally higher based on the earlier definition of leakage and subsequent

approximation via Fick's Law ($\vec{J}(\vec{r},E) = -D\nabla\Phi(\vec{r},E)$). The transport corrected diffusion coefficients are only derived based on the 11 mid-burnup cell one-dimensional problem and applied to all other cases with the intent of demonstrating the applicability of the values obtained using a simple model to more complex cases, thus avoiding the computational challenges in the form of CPU time and memory limitations when modelling larger geometries in deterministic transport codes.

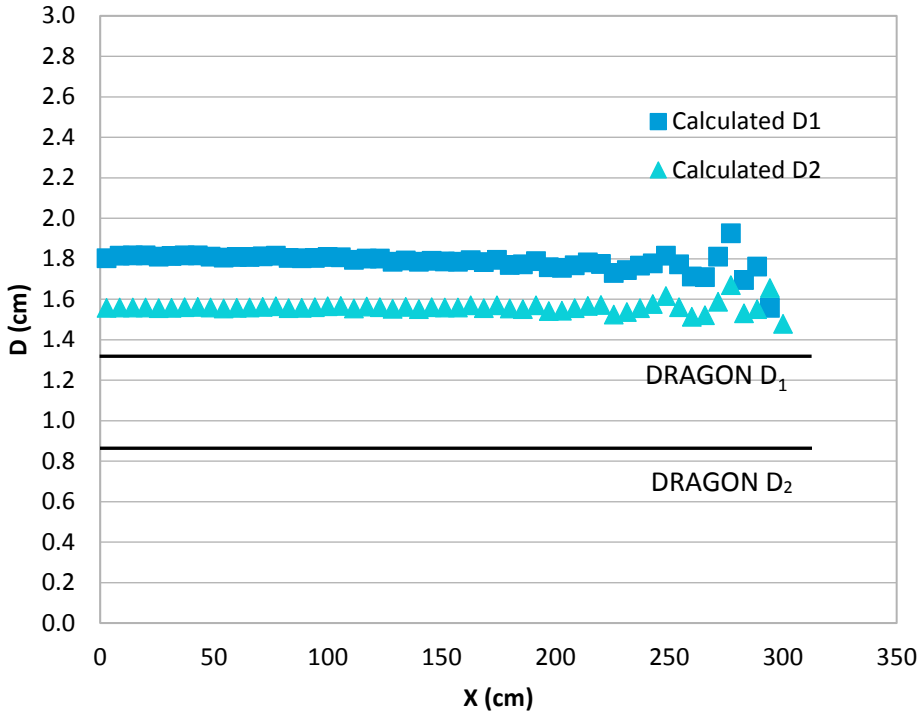

Figure 16: Spatial Dependence of One-Dimensional-Derived Diffusion Coefficients

The percent differences between DRAGON and DONJON results for the homogeneous 1-D case are shown in Figure 17. The flux percent differences confirm that the method is functioning as found in earlier work (Patel, 2010). It can be observed that the diffusion flux results fit closely the transport solution for the inner cells which are unaffected by the vacuum boundary condition, but near the vacuum boundary

condition the diffusion approximation breaks down for the nominal DONJON case, showing percent differences in flux of 5 – 7% for the cell homogenized fluxes. It is worthwhile to note that DONJON is under-predicting the flux for the cells near the vacuum boundary by up to 6% without the transport fitted coefficients. This means that there will be more neutrons leaking through the vacuum boundary in the uncorrected models. One would therefore predict that the k_{eff} values calculated by DONJON (especially without the transport correction) should be lower than those calculated by DRAGON since fewer neutrons are leaking out of the reactor.

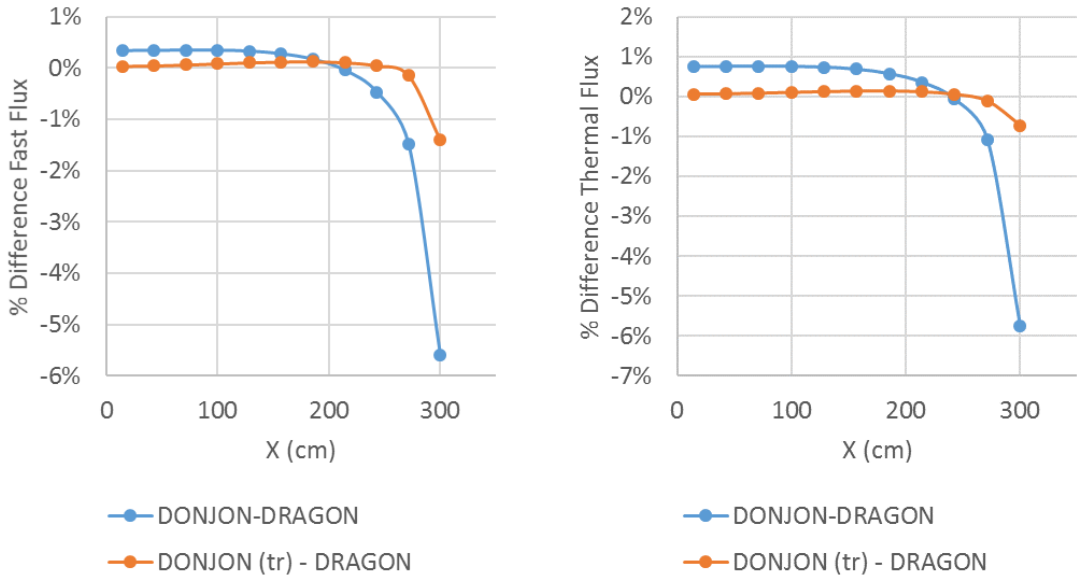

Figure 17: Percent Difference in Flux for the Homogeneous, 1-D Case

Upon applying the transport correction to the diffusion coefficient using the same corrected value across all cells, the percent differences between the flux values are reduced to less than 2% for the cell homogenized fluxes, calculated using Equation 52.

Figure 18 depicts the percent difference in fission rate; the DONJON diffusion results near the vacuum boundary condition is over six percent, but upon applying the transport corrected diffusion coefficients, this difference is reduced to less than one

percent, meaning bundle powers on the boundary of the reactor (near the edge) would be better predicted in models using the transport fitted coefficients.

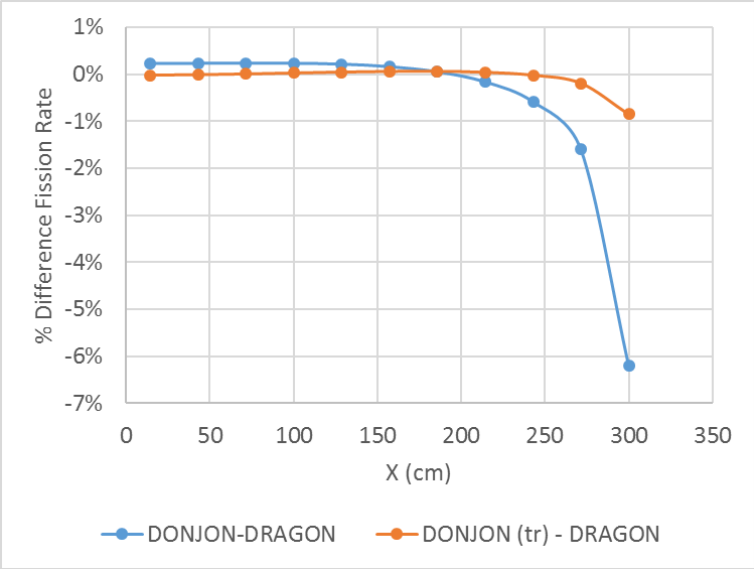

Figure 18: Percent Difference in Fission Rate for the Homogeneous, 1-D Case

The normalized flux values are plotted in Figure 19 for the thermal and fast fluxes, calculated using Equations 50 and 51. It can be observed from the flux plots that the curvature of the flux near the vacuum boundary condition is similar between the transport value and the diffusion results (for nominal and transport corrected cases). While the percent differences in fission rates and fluxes increase near the vacuum boundary condition, it is noted that overall the agreement between codes is quite good for this average mid-burnup model. The characteristic cosine shape of the flux in both cases is the usual shape for an infinite slab homogeneous reactor that is finite in one dimension.

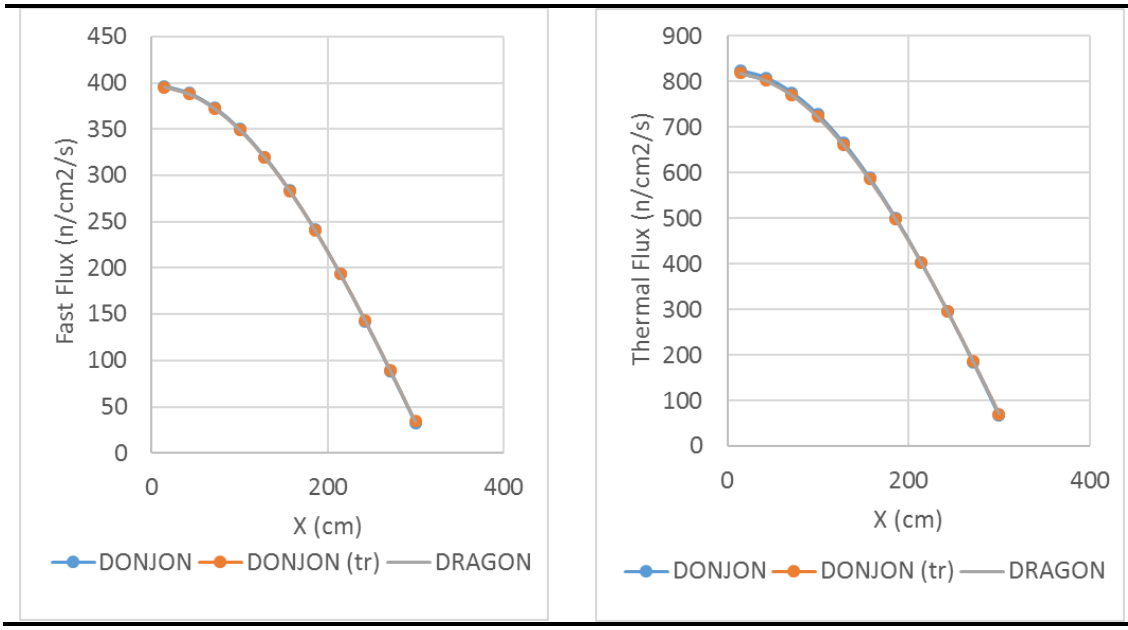

Figure 19: Flux for the Homogeneous, One-Dimensional Case

Table 4 provides a summary of the homogeneous 1-D case results. The higher k_{eff} value found by DONJON is reasonable given the flux percent difference results discussed earlier where a greater neutron flux near vacuum boundary in DRAGON models results in a lower k_{eff} value. It is good that the results obtained from DONJON have improved with the transport fitted diffusion coefficients, but it is somewhat expected because they have been fitted to this specific case.

Table 4: Results of Homogeneous, One-Dimensional Case

Parameter	DRAGON	DONJON	DONJON (tr)	Units
k_{eff}	1.04467	1.04984	1.04552	-
ρ	42.76	47.47	43.54	mk
Δρ	-	4.71	0.77	mk
Max % Difference Φ_1		-5.60	-1.40	%
Max % Difference Φ_2		-5.75	-0.72	%
RMS Error Φ_1		1.77	0.43	%
RMS Error Φ_2		1.86	0.24	%
Max % Difference Fission Rate		-6.20	-0.85	%

3.2 Homogeneous, One-Dimensional Coolant Voided Case

The next test is to examine the impact of a state change, namely coolant voiding, on the improvements made by using transport corrected diffusion coefficients found for the first case.

The results obtained for the voided case are summarized in Table 5, with clear improvements made in predictions of fission rate and flux similar to the ones observed for the cooled case previously analyzed. However, the k_{eff} value is better predicted by DONJON without the application of derived diffusion coefficients. How the k_{eff} value could be farther from the transport solution while fission rate and flux predictions are closer can be explained best by examining percent differences in fission rates for this case, given in Figure 20. The fission rate closely follows the behavior of the thermal flux and this profile is quite different from the results found for the cooled homogeneous, 1-D case studied earlier. The main issue with the transport corrected DONJON case seems to be the over prediction of neutron flux at the edge of the core relative to DRAGON, which would lead to more leakage and therefore reduced overall k_{eff} value in comparison to the transport solution. It appears as if the diffusion constants derived for the cooled mid-burnup case may be slightly too high to match the physics of the voided case. During coolant voiding the coolant is lost and therefore so is a source of neutron thermalization. Additionally, the neutrons that would have been thermalized near the fuel are more likely to be resonance absorbed in uranium-238. This increase in absorption contributes to a slight reduction in the diffusion coefficients (it translates into increased likelihood of reaction for neutrons while moving through a voided PT-HWR).

The uncorrected DONJON case is closer to the transport k_{eff} value, however this likely happens due to cancellation of errors rather than better prediction. The fission rate being significantly under-predicted at the edge of the core would lead to reduced leakage because there are fewer thermal neutrons at the vacuum boundary and more of them in the middle of the core causing fissions.

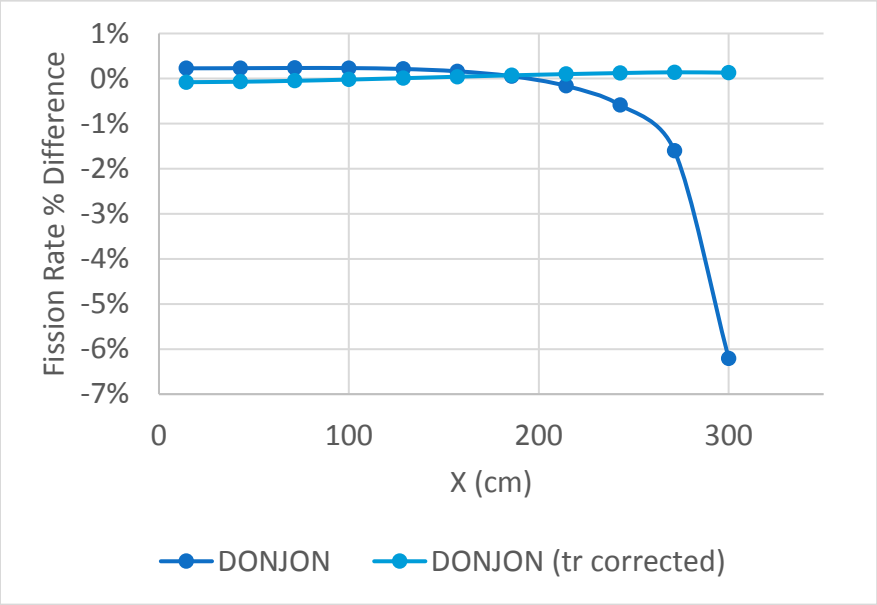

Figure 20: Fission Rate for Homogeneous, 1-D, Coolant Void Case

Table 5: Results of Homogeneous, 1-D Voided Case

Parameter	DRAGON	DONJON	DONJON (tr corrected)	Units
k_{eff}	1.06151	1.06258	1.05764	-
ρ	57.94	58.89	54.50	mk
Δρ	-	0.95	-3.44	mk
Max % Difference Φ_1		-6.33	-0.82	%
Max % Difference Φ_2		-6.10	-0.71	%
RMS Error Φ_1		2.10	0.71	%
RMS Error Φ_2		1.92	0.31	%
Max % Difference Fission Rate		-6.21	0.13	%

3.3 Heterogeneous, One-Dimensional Case

This heterogeneous case is the first one studied with reflector cells near the vacuum boundary condition. The combination of reflector and fresh fuel changes the flux shape from the characteristic cosine shape observed in the two homogeneous cases. This revised flux shape can be observed in Figure 21.

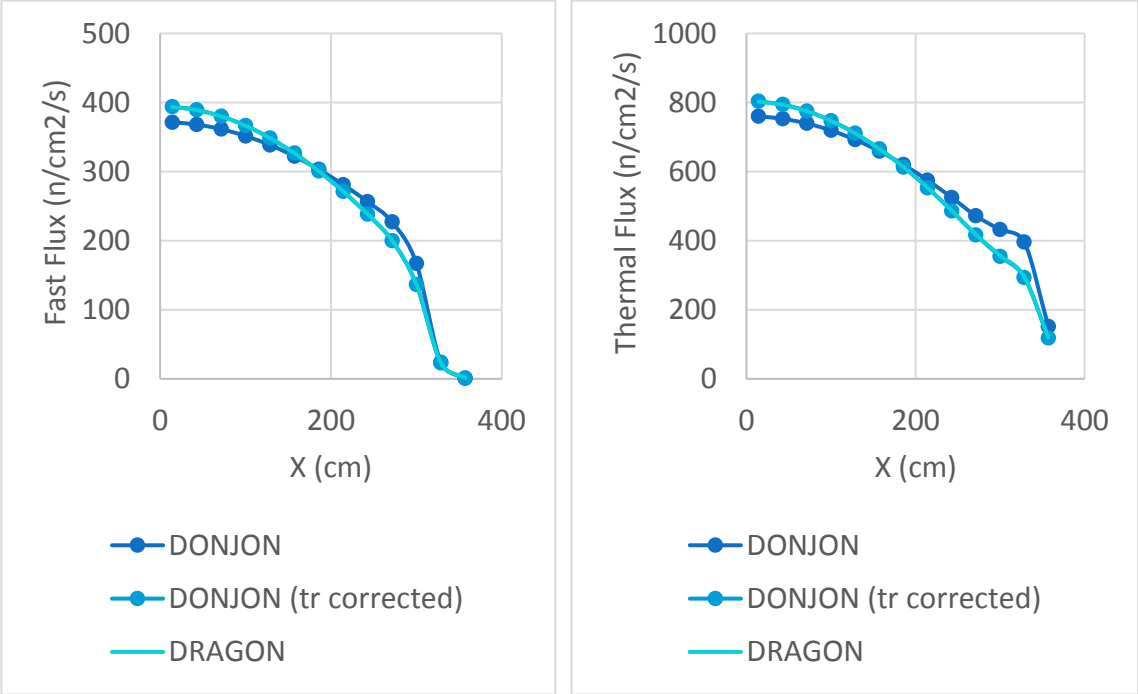

Figure 21: Flux for Heterogeneous, 1-D Case

The reason the fast flux drops to almost zero in the reflector cells is because the fast neutrons become thermalized in the heavy water reflector (note the increased thermal flux in the first cell of the reflector). Additionally, the curvature of the flux is shifted by having more reactive (fresh) fuel at the edge and highly depleted (exit-burnup) fuel in the centre of the model. The flux plots show a significant difference in the curvature of the flux between the nominal DONJON calculation and the DRAGON results. DONJON underestimates the flux values towards the centre of the core and

overestimates them near the reflector for the nominal diffusion coefficient results. The transport corrected diffusion coefficient flux values closely match the behavior of the DRAGON transport fluxes; despite being derived for a significantly simpler case with only one fuel type. Some physical meaning behind the different flux curvatures can be found once again by linking to the higher diffusion coefficients. In the regular DONJON case, the lower diffusion coefficient results in higher flux values in the fresh fuel (third node from the vacuum boundary), while in the DRAGON and transport fitted DONJON solutions, the flux values at the fresh fuel cell are lower. The general idea is that if the diffusion coefficient is low, the flux produced in the fresh fuel has a more challenging time dispersing in the model while higher coefficients allow those neutrons to move from region to region with less impedance. The value of the diffusion coefficient is particularly important in areas where the flux has a higher magnitude Laplacian as it is directly proportional to the calculated leakage. A plot of the DRAGON calculated flux Laplacian is shown in Figure 22 to provide clear insight into where significant changes occur, not surprisingly the inflection point happens at the interface between the fuel and the reflector.

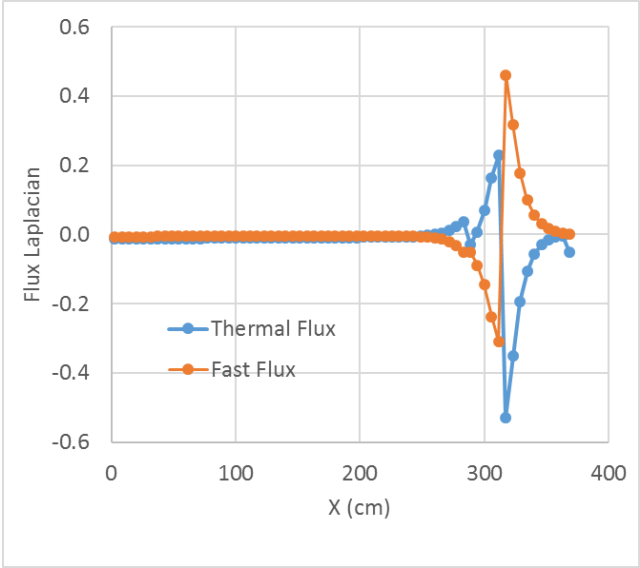

Figure 22: DRAGON Flux Laplacian for Heterogeneous, 1-D Case

Figure 23 shows the fast and thermal flux percent differences between DRAGON and DONJON. The fast flux has the largest difference in the reflector cell immediately adjacent to the vacuum boundary condition at 33%, while the thermal flux has the largest difference in the reflector cell adjacent to the fresh fuel of almost 35%.

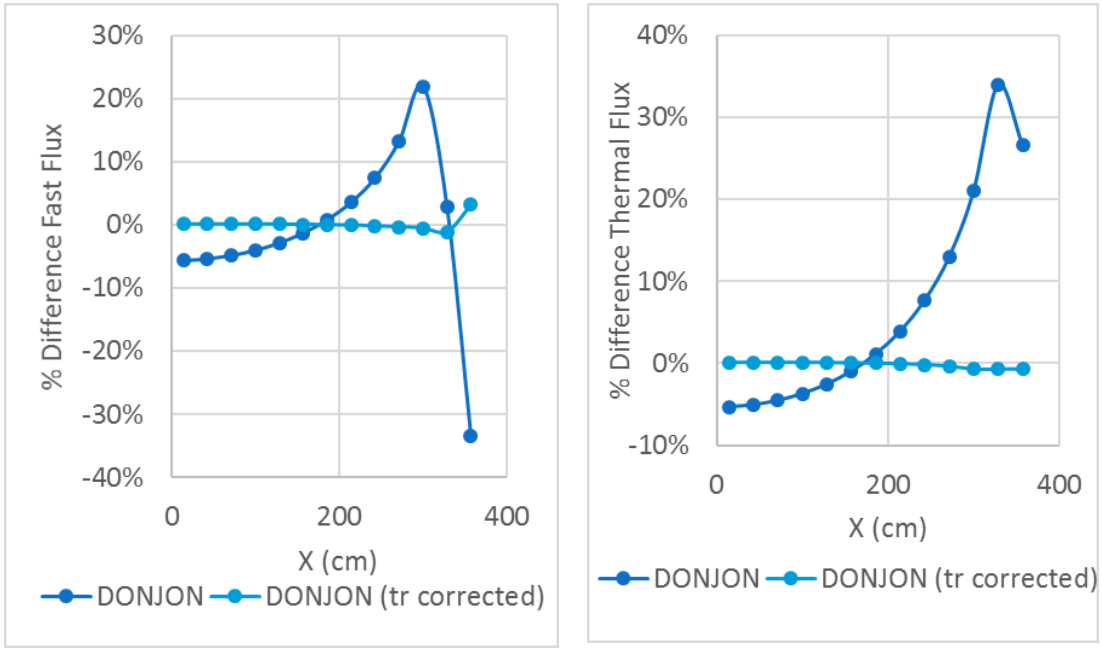

Figure 23: Percent Difference in Flux for Heterogeneous, 1-D Case

The fission rate percent difference between DRAGON and DONJON is given in Figure 24, with fissions being under-predicted in the center of the reactor and over predicted near the reflector (up to a maximum of 20% in the fresh fuel adjacent to the reflector). The diffusion case with transport corrected coefficients has a maximum fission rate percent difference that is almost negligible with a less than 1% difference in the fresh fuel.

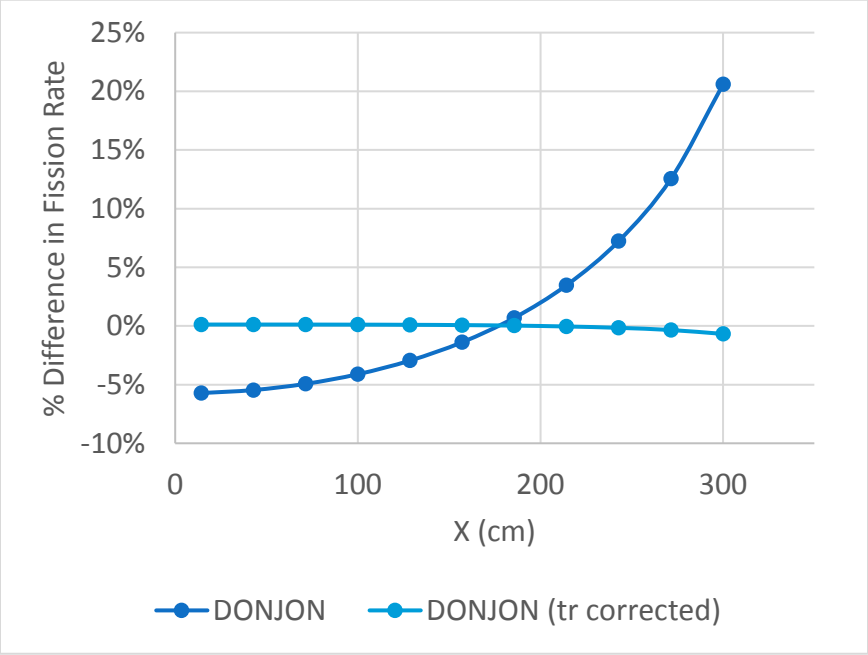

Figure 24: Percent Difference in Fission Rate for Heterogeneous, 1-D Case

Table 6 contains a summary of the transport and diffusion results obtained from this one dimensional, heterogeneous model. It is worthwhile to examine the improvements achieved for a similar case performed by (Patel, 2010) using BlackStallion, a diffusion solver written by Patel, given in Table 7. Similar reduction in the error between transport and diffusion are found in both studies, with more significant gains achieved in previous work, but this work achieves reductions that leave the differences

between diffusion and transport as almost negligible (maximum 3% flux error and less than 1% fission rate maximum error). The differences between this work and prior work show that it is worthwhile to re-evaluate published work with known code sets because the differences between transport and non-transport fitted diffusion calculations are significantly smaller in this re-evaluated study (~30% instead of ~150%).

Table 6: Results of Heterogeneous, One-Dimensional Case

Parameter	DRAGON	DONJON	$DONJON_{Tr\_Correct}$	Units
k_{eff}	1.00511	1.00903	1.00505	-
ρ	5.08	8.95	5.02	mk
Δρ	-	3.87	-0.06	mk
Max % Difference Φ_1		-33.43	3.18	%
Max % Difference Φ_2		33.95	-0.69	%
RMS Error Φ_1		8.71	0.20	%
RMS Error Φ_2		8.43	0.25	%
Max % Difference Fission Rate		20.61	-0.68	%

Table 7: BlackStallion Results for Heterogeneous, 1-D Case *(Patel, 2010)*

Parameter	BlackStallion	$BlackStallion_{Tr\_Correct}$	Units
RMS Error Φ_1	71.9	5.8	%
RMS Error Φ_2	80.5	4.5	%
Max % Difference Φ_1	129.2	15.3	%
Max % Difference Φ_2	173.1	0.14	%
Max % Difference Fission Rate	142.6	7.42	%

When moving to the heterogeneous and somewhat 'extreme' model detailed above, the burnup independence of the transport-fitted diffusion coefficient is demonstrated. At this point, it is worthwhile to move to more challenging cases and examine if the transport-derived diffusion coefficients for a stylized one-dimensional case can apply to two-dimensional models.

3.4 Heterogeneous, Two-Dimensional Case

The fast and thermal flux distribution obtained from DRAGON calculations for this case are shown in Figure 25 and Figure 26. The lowest flux values naturally occur at the mesh with the greatest leakage (the bottom right corner mesh with two vacuum boundaries). Similar flux curvatures occur in this 2-D model as those which appear in the heterogeneous 1-D model presented earlier, as is expected given their similar material and geometric configurations.

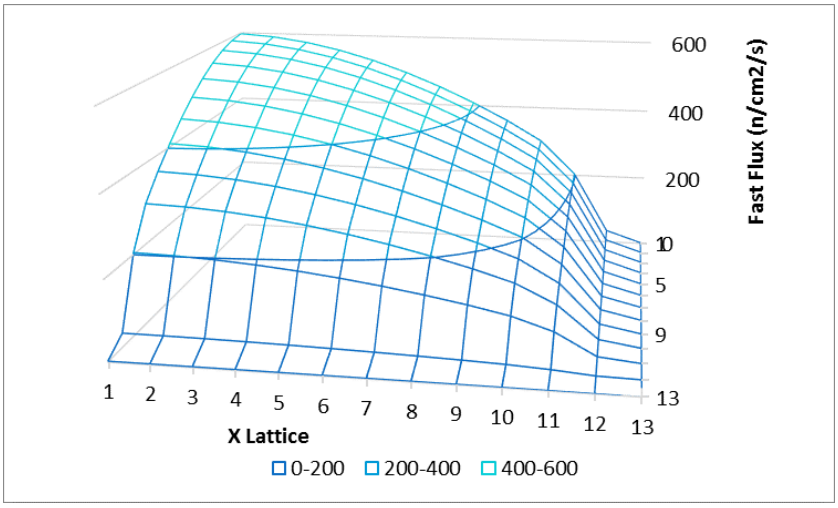

Figure 25: DRAGON Fast Flux for Heterogeneous, 2-D Case

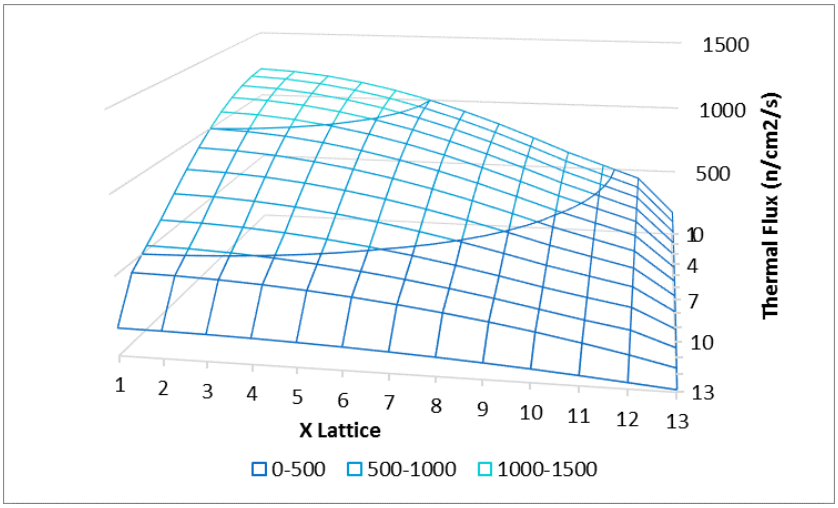

Figure 26: DRAGON Thermal Flux for Heterogeneous, 2-D Case

The fast flux percent differences for the normal and transport corrected DONJON cases compared with DRAGON are given in Figure 27 and Figure 28, respectively. For both transport corrected and nominal DONJON cases, the biggest fast flux discrepancies occur near the vacuum boundaries of the geometry, with the largest difference occurring in the bottom right corner. The transport correction as applied to the fast flux causes the percent differences to be reduced from 10% under-prediction to 0.2% over-prediction in the center and 37% under-prediction to 0.7% under-prediction in the bottom-right fresh fuel cell.

		X Mesh Centre Values (cm)												
		14	43	71	100	129	157	186	214	243	271	300	329	357
Y Mesh Centre Values (cm)	14	-10%	-10%	-9%	-9%	-8%	-6%	-4%	-2%	2%	7%	16%	-3%	-38%
	43	-10%	-10%	-9%	-8%	-7%	-6%	-4%	-1%	2%	8%	16%	-3%	-39%
	71	-9%	-9%	-9%	-8%	-7%	-5%	-4%	-1%	3%	8%	17%	-3%	-39%
	100	-9%	-8%	-8%	-7%	-6%	-5%	-3%	0%	3%	9%	17%	-2%	-39%
	129	-8%	-7%	-7%	-6%	-5%	-4%	-2%	1%	4%	10%	18%	-1%	-38%
	157	-6%	-6%	-5%	-5%	-4%	-2%	0%	2%	6%	11%	20%	0%	-37%
	186	-4%	-4%	-4%	-3%	-2%	0%	1%	4%	8%	13%	22%	1%	-36%
	214	-2%	-1%	-1%	0%	1%	2%	4%	6%	10%	15%	24%	3%	-35%
	243	2%	2%	3%	3%	4%	6%	8%	10%	13%	18%	27%	5%	-34%
	271	7%	8%	8%	9%	10%	11%	13%	15%	18%	23%	31%	8%	-32%
	300	16%	16%	17%	17%	18%	20%	22%	24%	27%	31%	37%	12%	-30%
	329	-3%	-3%	-3%	-2%	-1%	0%	1%	3%	5%	8%	12%	-6%	-35%
	357	-38%	-39%	-39%	-39%	-38%	-37%	-36%	-35%	-34%	-32%	-30%	-35%	-42%

Figure 27: DONJON Fast Flux Percent Differences for Heterogeneous, 2-D Case

		X Mesh Centre Values (cm)												
		14	43	71	100	129	157	186	214	243	271	300	329	357
Y Mesh Centre Values (cm)	14	0.2%	0.2%	0.2%	0.2%	0.2%	0.2%	0.1%	0.1%	0.0%	-0.2%	-0.4%	-1.6%	1.0%
	43	0.2%	0.2%	0.2%	0.2%	0.2%	0.2%	0.1%	0.1%	0.0%	-0.2%	-0.3%	-2.1%	-0.8%
	71	0.2%	0.2%	0.2%	0.2%	0.2%	0.2%	0.1%	0.1%	0.0%	-0.2%	-0.3%	-2.1%	-0.9%
	100	0.2%	0.2%	0.2%	0.2%	0.2%	0.2%	0.1%	0.1%	0.0%	-0.2%	-0.3%	-2.1%	-0.9%
	129	0.2%	0.2%	0.2%	0.2%	0.2%	0.2%	0.1%	0.1%	0.0%	-0.2%	-0.3%	-2.1%	-0.9%
	157	0.2%	0.2%	0.2%	0.2%	0.2%	0.2%	0.1%	0.0%	0.0%	-0.2%	-0.3%	-2.1%	-1.0%
	186	0.1%	0.1%	0.1%	0.1%	0.1%	0.1%	0.1%	0.0%	-0.1%	-0.2%	-0.3%	-2.2%	-1.0%
	214	0.1%	0.1%	0.1%	0.1%	0.1%	0.0%	0.0%	-0.1%	-0.1%	-0.3%	-0.4%	-2.2%	-1.0%
	243	0.0%	0.0%	0.0%	0.0%	0.0%	0.0%	-0.1%	-0.1%	-0.2%	-0.4%	-0.5%	-2.3%	-1.1%
	271	-0.2%	-0.2%	-0.2%	-0.2%	-0.2%	-0.2%	-0.2%	-0.3%	-0.4%	-0.5%	-0.6%	-2.4%	-1.1%
	300	-0.4%	-0.3%	-0.3%	-0.3%	-0.3%	-0.3%	-0.3%	-0.4%	-0.5%	-0.6%	-0.7%	-2.5%	-1.2%
	329	-1.6%	-2.1%	-2.1%	-2.1%	-2.1%	-2.1%	-2.2%	-2.2%	-2.3%	-2.4%	-2.5%	-3.7%	-3.1%
	357	1.0%	-0.8%	-0.9%	-0.9%	-0.9%	-1.0%	-1.0%	-1.0%	-1.1%	-1.1%	-1.2%	-3.1%	-4.8%

Figure 28: DONJON(tr) Fast Flux Percent Differences for Heterogeneous, 2-D Case

The maps of the thermal flux percent differences are given in Figure 29 and Figure 30. The flux results behave like the heterogeneous 1-D case; namely the flux predictions are significantly improved overall with the transport fitted diffusion coefficients, where DONJON moves from over-predicting the flux at the vacuum boundary condition to slightly under-predicting.

		X Mesh Centre Values (cm)												
		14	43	71	100	129	157	186	214	243	271	300	329	357
Y Mesh Centre Values (cm)	14	-10%	-9%	-9%	-8%	-7%	-6%	-4%	-1%	3%	8%	15%	27%	20%
	43	-9%	-9%	-9%	-8%	-7%	-5%	-3%	-1%	3%	8%	15%	28%	20%
	71	-9%	-9%	-8%	-7%	-6%	-5%	-3%	0%	3%	8%	16%	28%	21%
	100	-8%	-8%	-7%	-7%	-6%	-4%	-2%	0%	4%	9%	17%	29%	22%
	129	-7%	-7%	-6%	-6%	-5%	-3%	-1%	1%	5%	10%	18%	30%	23%
	157	-6%	-5%	-5%	-4%	-3%	-2%	0%	3%	6%	11%	19%	32%	24%
	186	-4%	-3%	-3%	-2%	-1%	0%	2%	5%	8%	13%	21%	33%	26%
	214	-1%	-1%	0%	0%	1%	3%	5%	7%	10%	15%	23%	36%	28%
	243	3%	3%	3%	4%	5%	6%	8%	10%	14%	18%	26%	38%	30%
	271	8%	8%	8%	9%	10%	11%	13%	15%	18%	22%	29%	41%	33%
	300	15%	15%	16%	17%	18%	19%	21%	23%	26%	29%	33%	43%	34%
	329	27%	28%	28%	29%	30%	32%	33%	36%	38%	41%	43%	41%	33%
	357	20%	20%	21%	22%	23%	24%	26%	28%	30%	33%	34%	33%	25%

Figure 29: DONJON Thermal Flux Percent Difference for Heterogeneous, 2-D Case

		X Mesh Centre Values (cm)												
		14	43	71	100	129	157	186	214	243	271	300	329	357
Y Mesh Centre Values (cm)	14	0.2%	0.2%	0.2%	0.2%	0.2%	0.2%	0.1%	0.1%	0.0%	-0.2%	-0.6%	-0.8%	-1.0%
	43	0.2%	0.2%	0.2%	0.2%	0.2%	0.2%	0.1%	0.1%	0.0%	-0.2%	-0.6%	-0.9%	-1.0%
	71	0.2%	0.2%	0.2%	0.2%	0.2%	0.2%	0.1%	0.1%	0.0%	-0.2%	-0.6%	-0.9%	-1.1%
	100	0.2%	0.2%	0.2%	0.2%	0.2%	0.2%	0.1%	0.1%	0.0%	-0.2%	-0.6%	-0.9%	-1.1%
	129	0.2%	0.2%	0.2%	0.2%	0.2%	0.2%	0.1%	0.1%	0.0%	-0.2%	-0.7%	-0.9%	-1.1%
	157	0.2%	0.2%	0.2%	0.2%	0.2%	0.1%	0.1%	0.0%	-0.1%	-0.2%	-0.7%	-0.9%	-1.1%
	186	0.1%	0.1%	0.1%	0.1%	0.1%	0.1%	0.1%	0.0%	-0.1%	-0.3%	-0.7%	-1.0%	-1.2%
	214	0.1%	0.1%	0.1%	0.1%	0.1%	0.0%	0.0%	-0.1%	-0.2%	-0.3%	-0.8%	-1.0%	-1.2%
	243	0.0%	0.0%	0.0%	0.0%	0.0%	-0.1%	-0.1%	-0.2%	-0.2%	-0.4%	-0.8%	-1.1%	-1.3%
	271	-0.2%	-0.2%	-0.2%	-0.2%	-0.2%	-0.2%	-0.3%	-0.3%	-0.4%	-0.6%	-1.0%	-1.2%	-1.4%
	300	-0.6%	-0.6%	-0.6%	-0.6%	-0.7%	-0.7%	-0.7%	-0.8%	-0.8%	-1.0%	-1.3%	-1.4%	-1.5%
	329	-0.8%	-0.9%	-0.9%	-0.9%	-0.9%	-0.9%	-1.0%	-1.0%	-1.1%	-1.2%	-1.4%	-1.6%	-1.6%
	357	-1.0%	-1.0%	-1.1%	-1.1%	-1.1%	-1.1%	-1.2%	-1.2%	-1.3%	-1.4%	-1.5%	-1.6%	-1.6%

Figure 30: DONJON (tr) Thermal Flux Percent Difference for Heterogeneous, 2-D Case

The maps of the fission rate percent differences are provided in Figure 31 and Figure 32. As fission rate is strongly related to the thermal flux, similar results are exhibited.

Y Mesh Centre Value (cm) \ X mesh centre value (cm)	14	43	71	100	129	157	186	214	243	271	300	329	357
14	-10%	-10%	-10%	-9%	-8%	-6%	-4%	-2%	2%	7%	14%	0%	0%
43	-10%	-10%	-9%	-9%	-8%	-6%	-4%	-2%	2%	7%	14%	0%	0%
71	-10%	-9%	-9%	-8%	-7%	-6%	-4%	-1%	2%	7%	15%	0%	0%
100	-9%	-9%	-8%	-7%	-6%	-5%	-3%	0%	3%	8%	16%	0%	0%
129	-8%	-8%	-7%	-6%	-5%	-4%	-2%	1%	4%	9%	17%	0%	0%
157	-6%	-6%	-6%	-5%	-4%	-3%	-1%	2%	5%	10%	18%	0%	0%
186	-4%	-4%	-4%	-3%	-2%	-1%	1%	4%	7%	12%	20%	0%	0%
214	-2%	-2%	-1%	0%	1%	2%	4%	6%	10%	14%	22%	0%	0%
243	2%	2%	2%	3%	4%	5%	7%	10%	13%	17%	25%	0%	0%
271	7%	7%	7%	8%	9%	10%	12%	14%	17%	21%	28%	0%	0%
300	14%	14%	15%	16%	17%	18%	20%	22%	25%	28%	32%	0%	0%
329	0%	0%	0%	0%	0%	0%	0%	0%	0%	0%	0%	0%	0%
357	0%	0%	0%	0%	0%	0%	0%	0%	0%	0%	0%	0%	0%

Figure 31: DONJON Fission Rate Percent Differences for Heterogeneous, 2-D Case

Y Mesh Centre Values (cm) \ X Mesh Centre Values (cm)	14	43	71	100	129	157	186	214	243	271	300	329	357
14	0.2%	0.2%	0.2%	0.2%	0.2%	0.2%	0.1%	0.1%	0.0%	-0.2%	-0.6%	0.0%	0.0%
43	0.2%	0.2%	0.2%	0.2%	0.2%	0.2%	0.1%	0.1%	0.0%	-0.2%	-0.6%	0.0%	0.0%
71	0.2%	0.2%	0.2%	0.2%	0.2%	0.2%	0.1%	0.1%	0.0%	-0.2%	-0.6%	0.0%	0.0%
100	0.2%	0.2%	0.2%	0.2%	0.2%	0.2%	0.1%	0.1%	0.0%	-0.2%	-0.6%	0.0%	0.0%
129	0.2%	0.2%	0.2%	0.2%	0.2%	0.2%	0.1%	0.1%	0.0%	-0.2%	-0.6%	0.0%	0.0%
157	0.2%	0.2%	0.2%	0.2%	0.2%	0.1%	0.1%	0.0%	-0.1%	-0.2%	-0.7%	0.0%	0.0%
186	0.1%	0.1%	0.1%	0.1%	0.1%	0.1%	0.1%	0.0%	-0.1%	-0.3%	-0.7%	0.0%	0.0%
214	0.1%	0.1%	0.1%	0.1%	0.1%	0.0%	0.0%	-0.1%	-0.2%	-0.3%	-0.7%	0.0%	0.0%
243	0.0%	0.0%	0.0%	0.0%	0.0%	-0.1%	-0.1%	-0.2%	-0.3%	-0.4%	-0.8%	0.0%	0.0%
271	-0.2%	-0.2%	-0.2%	-0.2%	-0.2%	-0.2%	-0.3%	-0.3%	-0.4%	-0.6%	-1.0%	0.0%	0.0%
300	-0.6%	-0.6%	-0.6%	-0.6%	-0.6%	-0.7%	-0.7%	-0.7%	-0.8%	-1.0%	-1.3%	0.0%	0.0%
329	0.0%	0.0%	0.0%	0.0%	0.0%	0.0%	0.0%	0.0%	0.0%	0.0%	0.0%	0.0%	0.0%
357	0.0%	0.0%	0.0%	0.0%	0.0%	0.0%	0.0%	0.0%	0.0%	0.0%	0.0%	0.0%	0.0%

Figure 32: DONJON (tr) Fission Rate Percent Difference for Heterogeneous 2-D Case

The RMS difference in fast flux between DRAGON and DONJON is given in Table 8. Applying the transport correction to the fast flux results in an RMS percent difference reduction from ~17% to less than 1% for both the fast and thermal fluxes. The reactivity difference between DRAGON and DONJON has been reduced from almost 8 mk to less than 0.1 mk by applying the transport fitted diffusion coefficients while significantly

improving the spatial flux agreement. Similarly, fission rate RMS error is reduced from 10% to less than 0.5%. The 2-D application of 1-D derived coefficients seems adequate given these results.

Table 8: Results Summary for Heterogeneous, 2-D Case

	DRAGON	DONJON	DONJON (tr corrected)	Units
k_{eff}	0.997245	1.005192	0.997326	-
ρ	-2.76	5.16	-2.68	mk
Δρ		7.93	0.08	mk
Max % Difference Φ_1		17.2	0.00	%
Max % Difference Φ_2		18.7	0.69	%
RMS Error Φ_1		41.7	4.8	%
RMS Error Φ_2		42.7	1.6	%
Max % Difference Fission Rate		31.7	1.3	%
Fission Rate RMS		10.8	0.36	%

3.5 Heterogeneous, Three-Dimensional Case

The DONJON results for the fast flux are given in Table 9-Table 10. Once again, the largest fast flux differences between DRAGON and DONJON occur in the reflector regions. The overall errors made by DONJON without the transport fitted diffusion coefficients are not as large as in the 2-D case, but review Table 3 to recall that the fuel to surface area ratio of this model is a significant departure from previous modelling efforts (significantly larger vacuum boundary surface area in comparison to other models). Additionally, this model is the only one built where the volume of reflector is larger than the volume of the fuel. Both factors contribute to the significant sub-criticality of the model (seen in Table 15). Recall the reason for this change is due to the relative size of the model that is achievable given memory limitations in DRAGON. In

Table 11 and Table 12 the percent differences in thermal flux are given. Note that for all models, corrected and nominal DONJON, they are quite close to the DRAGON predictions (except in the reflector region).

Table 9: Fast Flux % Difference from DONJON for 3D Heterogeneous Case

			X Mesh Centre Values (cm)		
			14.28	42.87	71.44
			Z=24.76 cm		
			Exit	Fresh	Refl
Y-Mesh Centre Values (cm)	14.28	Exit	10.04%	7.44%	23.02%
	42.87	Fresh	7.44%	5.49%	22.58%
	71.44	Refl	23.02%	22.58%	35.33%
			Z=74.29 cm		
			Fresh	Fresh	Refl
	14.28	Fresh	10.20%	7.76%	23.47%
	42.87	Fresh	7.76%	5.67%	22.94%
	71.44	Refl	23.47%	22.94%	35.84%
			Z=123.83 cm		
			Refl	Refl	Refl
	14.28	Refl	21.63%	20.93%	34.00%
	42.87	Refl	20.93%	20.40%	34.42%
	71.44	Refl	34.00%	34.42%	44.56%

Table 10: Fast Flux % Difference from DONJON(tr) for 3D Heterogeneous Case

			X Mesh Centre Values (cm)		
			14.28	42.87	71.44
			Z=24.76 cm		
			Exit	Fresh	Refl
Y-Mesh Centre Values (cm)	14.28	Exit	2.21%	2.35%	0.73%
	42.87	Fresh	2.35%	2.46%	0.20%
	71.44	Refl	0.73%	0.20%	-1.61%
			Z=74.29 cm		
			Fresh	Fresh	Refl
	14.28	Fresh	0.34%	0.46%	-1.16%
	42.87	Fresh	0.46%	0.87%	-1.48%
	71.44	Refl	-1.16%	-1.48%	-3.42%
			Z=123.83 cm		
			Refl	Refl	Refl
	14.28	Refl	4.07%	3.35%	1.70%
	42.87	Refl	3.35%	2.88%	0.61%
	71.44	Refl	1.70%	0.61%	-1.40%

Table 11: Thermal Flux % Difference from DONJON for 3D Heterogeneous Case

			X Mesh Centre Values (cm)		
			14.28	42.87	71.44
			Z=24.76 cm		
			Exit	Fresh	Refl
Y-Mesh Centre Values (cm)	14.28	Exit	0.78%	-2.37%	-7.31%
	42.87	Fresh	-2.37%	-3.57%	-6.93%
	71.44	Refl	-7.31%	-6.93%	-1.82%
			Z=74.29 cm		
			Fresh	Fresh	Refl
	14.28	Fresh	4.32%	-0.82%	-6.03%
	42.87	Fresh	-0.82%	-2.55%	-5.78%
	71.44	Refl	-6.03%	-5.78%	-0.75%
			Z=123.83 cm		
			Refl	Refl	Refl
	14.28	Refl	-6.23%	-7.31%	-3.15%
	42.87	Refl	-7.31%	-7.42%	-2.57%
	71.44	Refl	-3.15%	-2.57%	3.00%

Table 12: Thermal Flux % Difference from DONJON (tr) for 3D Heterogeneous Case

			X Mesh Centre Values (cm)		
			14.28	42.87	71.44
			Z=24.76 cm		
			Exit	Fresh	Refl
Y-Mesh Centre Values (cm)	14.28	Exit	1.16%	1.18%	0.84%
	42.87	Fresh	1.18%	0.97%	0.57%
	71.44	Refl	0.84%	0.57%	-0.02%
			Z=74.29 cm		
			Fresh	Fresh	Refl
	14.28	Fresh	-3.60%	-1.22%	-0.61%
	42.87	Fresh	-1.22%	-0.69%	-0.67%
	71.44	Refl	-0.61%	-0.67%	-1.07%
			Z=123.83 cm		
			Refl	Refl	Refl
	14.28	Refl	-1.48%	-0.69%	-0.27%
	42.87	Refl	-0.69%	-0.38%	-0.29%
	71.44	Refl	-0.27%	-0.29%	-0.48%

Table 13: Fission Rate Difference from DONJON for 3D Heterogeneous Case

			X Mesh Centre Values (cm)		
			14.28	42.87	71.44
			Z=24.76 cm		
			Exit	Fresh	Refl
Y-Mesh Centre Values (cm)	14.28	Exit	-1.65%	1.55%	0.00%
	42.87	Fresh	1.55%	2.89%	0.00%
	71.44	Refl	0.00%	0.00%	0.00%
			Z=74.29 cm		
			Fresh	Fresh	Refl
	14.28	Fresh	-4.84%	0.15%	0.00%
	42.87	Fresh	0.15%	1.97%	0.00%
	71.44	Refl	0.00%	0.00%	0.00%
			Z=123.83 cm		
			Refl	Refl	Refl
	14.28	Refl	0.00%	0.00%	0.00%
	42.87	Refl	0.00%	0.00%	0.00%
	71.44	Refl	0.00%	0.00%	0.00%

Table 14: Fission Rate Difference from DONJON(tr) for 3D Heterogeneous Case

			X Mesh Centre Values (cm)		
			14.28	42.87	71.44
			Z=24.76 cm		
			Exit	Fresh	Refl
Y-Mesh Centre Values (cm)	14.28	Exit	1.26%	1.28%	0.00%
	42.87	Fresh	1.28%	1.08%	0.00%
	71.44	Refl	0.00%	0.00%	0.00%
			Z=74.29 cm		
			Fresh	Fresh	Refl
	14.28	Fresh	-3.26%	-1.09%	0.00%
	42.87	Fresh	-1.09%	-0.58%	0.00%
	71.44	Refl	0.00%	0.00%	0.00%
			Z=123.83 cm		
			Refl	Refl	Refl
	14.28	Refl	0.00%	0.00%	0.00%
	42.87	Refl	0.00%	0.00%	0.00%
	71.44	Refl	0.00%	0.00%	0.00%

Table 15: Results of Three-Dimensional, Heterogeneous Case

	DRAGON	DONJON	DONJON (tr corrected)	Units
k_{eff}	0.722770	0.827437	0.715954	-
ρ	-383.6	-208.5	-396.7	mk
Δρ		175.0	-13.2	mk
Max % Difference Φ_1		44.6	4.1	%
Max % Difference Φ_2		7.4	3.6	%
RMS Error Φ_1		21.5	0.85	%
RMS Error Φ_2		4.8	1.0	%
Max % Difference Fission Rate		4.8	3.3	%
Fission Rate RMS		1.26	0.85	%

The fission rate percent differences are given in Table 13 and Table 14. The fission rate differences are only slightly improved by applying the transport fitted diffusion coefficients (maximum of 5% reduced to 3%). DONJON has challenges with modelling this system which can be summarized in Table 15. DONJON results in a

175 mk difference in reactivity between models. When applying the corrected diffusion coefficients, this large difference is reduced by over 90% to a 13 mk difference. The RMS fast flux errors are reduced from 21% for the nominal case to less than 1%, while maximum fast flux percent difference is reduced from 44% to 4-5%. The thermal flux and the fission rate error is only slightly improved. This is likely due to the small amount of fuel involved in the model as the fluxes of each model are normalized to match the total fission rate. It is expected that in larger problems the fission rate error would be larger, and therefore the application of the transport correction to the diffusion coefficient will result in greater improvement.

4. CONCLUSIONS

Calculations to confirm the improvement of flux and fission rate calculations by transport fitted diffusion coefficients in 1D and 2D by Patel (2010) were performed using the code pair DRAGON/DONJON. Patel's work was also extended to demonstrate the efficacy of transport corrected diffusion coefficient for three-dimensional models. The advantage of this method of homogenization is its ease of application. It was shown that diffusion coefficients derived using a simple 1D case with homogeneous mid-burnup fuel can be applied to a number of different problems with differing geometries and significant flux gradients. Though a simple 11 cell case is used to find diffusion coefficients, the results of 1-D, 2-D and 3-D heterogeneous models are improved significantly. The cell averaged fluxes and k_{eff} for the 3-D case show excellent agreement, with a maximum difference in reactivity of 15 mk and a 4% maximum difference in local flux in comparison to 175 mk and 44% for the non-transport fitted diffusion coefficient DONJON case.

This method of adjusting the diffusion coefficient based on transport results may be a means to achieve better agreement between transport codes and diffusion codes for heavy water type reactors.

Future work of interest is to derive diffusion coefficients based on WIMS-AECL (Altiparmakov D. V., 2008) depletion data and apply them to RFSP (Rouben B. , 1995) calculations as per the industry standard methods to compare with known correction methods using multi-cell tables to simulate the reflector region (Altiparmakov & Shen,

2013). The simplicity in the method lends itself to implementation in older codes where more complex improvement methods would be challenging to use.

5. REFERENCES

Altiparmakov, D. V. (2008). New Capabilities of the Lattice Code WIMS-AECL. *International Conference on the Physics of Reactors.* Interlaken, Switzerland: American Nuclear Society.

Altiparmakov, D., & Shen, W. (2013). Multicell Correction Method for Treatment of Heterogeneities in Full-Core Calculation of CANDU-Type Reactors". *Nuclear Science and Engineering*, 109-134.

Brown, F. B. (2002). *MCNP Version 5.* Los Alamos: Los Alamos National Laboratory.

Chadwick, M. B. (2011). *ENDF/B-VII.1: Nuclear Data for Science and Technology: Cross Sections, Covariances, Fission Product Yields and Decay Data.* Nucl. Data Sheets.

Hangbok, C., Gyuhong, R., & Donghwan, P. (2005). Benchmarking MCNP and WIMS/RFSP against measurement data - II: Wolsong nuclear power plant 2. *Nuclear Science and Engineering*.

Marleau, G., Herbert, A., & Roy, R. (2013). *A User Guide for DRAGON Release 3.06L.* Montreal: Ecole Polytechnique de Montreal.

Page, R. (2012, 3 2). *Image Library*. Retrieved from CANTEACH: https://canteach.candu.org/Image%20Library1/Forms/DispForm.aspx?ID=203

Patel, A. (2010). *Transport-Theory-Equivalent Diffusion Coefficients for Node-Homogenized Neutron DIffusion Problems in CANDU Lattices.* Oshawa: University of Ontario Institute of Technology.

Rosana, M. (2014, June). *CANDU: A Canadian Success Story*. Retrieved from Canadian Geographic: httwww.canadiangeographic.ca/magazine/jun14/candu-nuclear-reactor-canadian-success-story.asp

Rouben, B. (1995). Overview of current RFSP-code capabilities for CANDU core analysis. *Transactions of the American Nuclear Society*, 25-29.

Rouben, B., & Nichita, E. (2016). Reactor Statics. In W. Garland, *The Essential CANDU: A Textbook on the CANDU Nuclear Power Plant Technology* (p. 36). Hamilton: UNENE.

Varin, E., Hebert, A., Roy, R., & Koclas, J. (2005). *A User Guide for DONJON Version 3.01.* Montreal: Institut de genie nucleaire, Ecole Polytechnique de Montreal.

WIMS Library Update. (2016, February 12). Retrieved from International Atomic Energy Agency Nuclear Data Services: https://www-nds.iaea.org/wimsd/

Yasin, Z., Iqbal, J., & Shahzad, I. M. (2011). Comparison of Radionuclide's Inventories and Activities with Slightly Enriched Uranium and Plutonium Fuel in CANDU Reactors. *World Journal of Nuclear Science and Technology*, 31-36.

APPENDIX A: MESH REFINEMENT STUDY

X Mesh Convergence Study

A convergence study is performed to the one-dimensional homogenized transport models that are used to both derive and test the diffusion coefficients. The metric by which convergence is judged is k_{eff}. The test case consists of a one-dimensional model (like the 1-D homogeneous case used to derive the diffusion coefficients) with one fuel type (mid-burnup) and 11 lattice cells. The model is prepared in the transport code DRAGON to evaluate at what point the mesh spacing is adequate. The meshes that are used in this study refer to the number of meshes in the x direction in a single lattice cell. The results of the x-mesh convergence study are given in Figure 33.

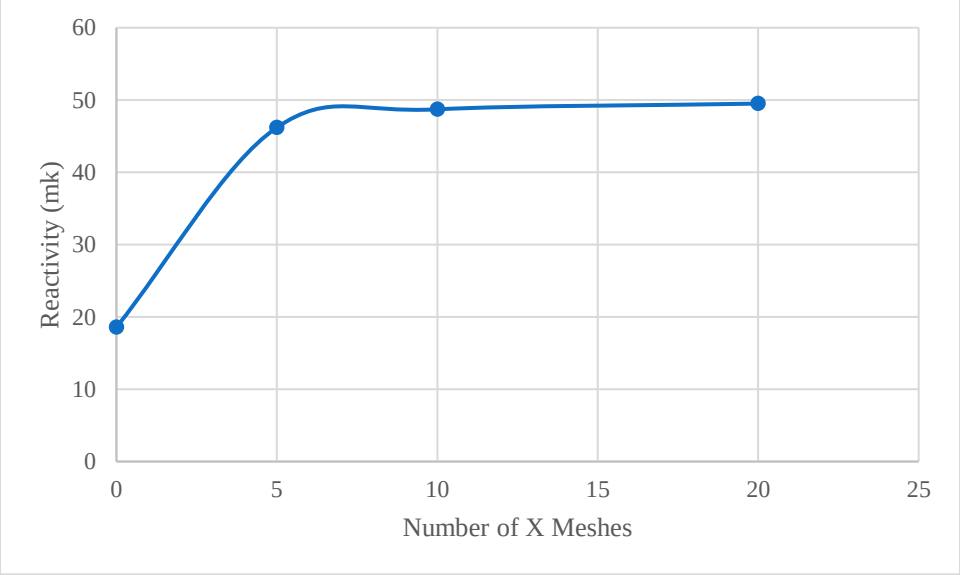

Figure 33: X Mesh Convergence Study in DRAGON

Due to memory limitations in moving to 3-D models, a compromise is made and the 5 mesh model is chosen to provide adequate k_{eff} convergence while allowing enough

memory for larger 3D models. As the y dimension of the lattice cell is equal to the x-dimension the number of meshes chosen for x are applied to y in all models.

Z-Mesh Convergence Study

A similar 1-D DRAGON model is set up based on the model used for the x-mesh study above with the exception that it is in the Y-Z plane. The model contains 5 meshes for the y dimension of the lattice and the number of z-meshes in a single cell are varied. The difference in the z-mesh convergence study is that one lattice pitch in the y-direction and six bundle lengths in the z-direction are used (49.53 cm each) with a vacuum boundary condition applied to the positive z axis and reflective boundary conditions elsewhere. The resultant reactivity values are given in Figure 34 and show that the reactivity converges nicely with 20 meshes, similar to the x mesh study a compromise is made and 10 meshes are chosen.

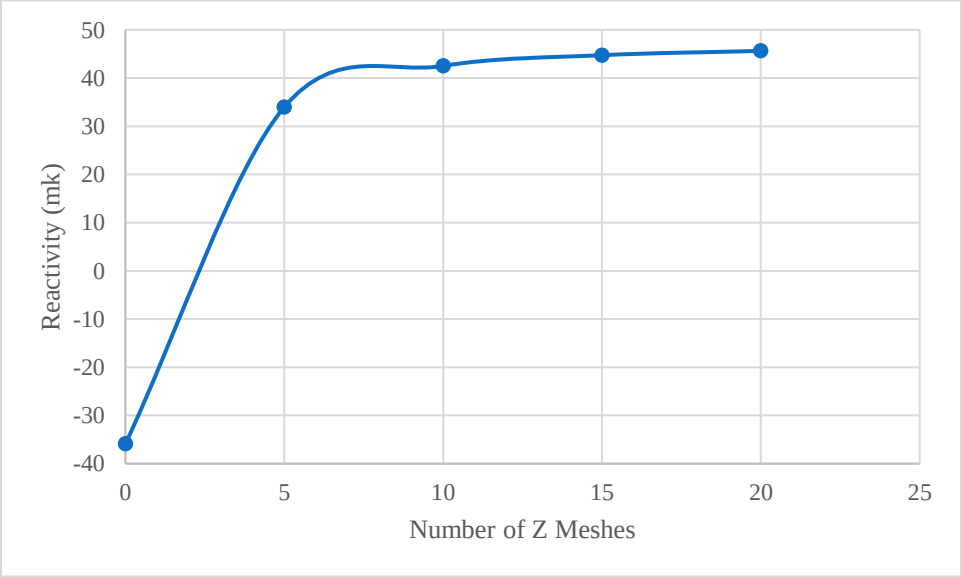

Figure 34: Z-Mesh Convergence Study in DRAGON